ELECTRICAL DECAY ESTIMATES IN ANVIL CLOUDS
Report No. 3 -- Final Report under Contract No. CC-90796B
John C. Willett, 10/31/03

Introduction

A simple model of the decay of pre-existing electrification in anvil clouds was developed under an earlier contract, CC-90233B [*Willett*, 2001, 2003; *Willett and Dye*, 2003]. This is the only and final report under a follow-on contract to validate that model to the extent practicable using the ABFM 2000 - 2001 dataset. Additional results of the application of the model to the that dataset have been described by *Dye et al*. [2002, 2003]. This project was undertaken to aid NASA and the USAF in determining when such clouds do not constitute a triggered-lightning hazard for either an outgoing launch vehicle or a landing Space Shuttle. Both a statistical approach, using data from all suitable anvil penetrations, and a case-study approach, using only selected anvil clouds, are employed herein.

Relation of Electrical Decay Time to Other Measurements

This section considers statistical relationships among some of the parameters in the "30-s Merged Files" that are currently available on the NCAR ABFM Web site. These files give 30 s averages of many parameters that were measured, both aboard the ABFM aircraft and by the two ground-based radars, during the aircraft flights. Also given in these files are the corresponding values of numerous derived quantities, such as the "electrical-decay time scale" from the model, τ_E, and the radar reflectivity averaged (in dBZ) over a volume 3 km on a side centered on the aircraft location, R_3. In particular, we examine τ_E (called ETmScl in the 30-s Merged Files), the magnitude of the vector electrostatic field at the aircraft, $|\boldsymbol{E}|$ (called Em_m), R_3 (called AVGCUBE3X3), and cloud-particle concentrations in four size ranges -- between about 3 and about 55 μm diameter from the FSSP instrument, $N_{3\text{-}55}$ (called Con_FSSP), between 100 and 200 μm diameter from the 2D-C probe, $N_{100\text{-}200}$ (called 2DC_100_200), between 200 and 1000 μm diameter from the 2D-C, $N_{200\text{-}1000}$ (called 2DC_200_1000), larger than 1000 μm diameter from the 2D-C, $N_{>1000}$ (called 2DC_GT_1000), and larger than 1000 μm diameter from the HVPS instrument, $N'_{>1000}$ (called HVPS_GT_1000). The primary goals of this exercise are (1) to show how τ_E depends on the particle-size distribution and is (or is not) related to the radar

reflectivity and (2) to search for evidence that τ_E can be used as an indicator of $|\boldsymbol{E}|$.

We begin with several comments about methodology:

1) Radar data and products from the WSR-74C have been used whenever possible. Of the 16 flights that contain NCAR-designated anvil passes, however, only NEXRAD data are available for one (000613 -- YYMMDD) and the WSR-74C suffered precipitation and/or wet-radome attenuation during some portion of the anvil passes on four others (010602, 010610, 010624, and 010627). In all of these intervals NEXRAD data were simply substituted for WSR-74C.

2) In the one case where radar grid 2 placed the anvil further from the edge of the grid box (case 2 on 010525), grid 2 data were substituted for those from grid 1.

3) In order to confine attention to true anvils, all cases with "Anvil_Type" = 0 (as defined by NCAR) were deleted.

4) In an attempt to assure that the aircraft was actually inside the anvil, we required that the flight level (POSAlt) ≥ 5 km, $\tau_E \geq 20$ s, and $\tau_E \neq$ "NaN" (the NCAR symbol for no data).

5) At this point only five cases remained with $|\boldsymbol{E}|$ = "NaN", so these were deleted as well, leaving a total of 2190 cases (30-s intervals) for analysis. This dataset was designated "minflt" and formed the basis for all further analysis.

Dependence of τ_E and R_3 on Particle Distributions

Before looking at these statistical relationships, it is instructive to return, for a moment, to the particle-size distributions themselves and their theoretical relationships to τ_E and R_3. Figure 1 shows the measured size distribution that was used as an example by *Willett and Dye* [2003]. Figure 2 compares the corresponding spectra of diffusive-loss rate (in red) and of field-driven-attachment loss rate (green) of small ions to cloud particles. This figure is identical to *Willett and Dye* [2003, Fig.2] except that here we have over-plotted in blue the spectrum of relative contribution to the radar reflectivity (which goes as d^6), computed from the same size distribution. (The model parameters for this case are τ_E = 5963 s, $E_.$ = 551 V/m, and τ_D = 66 s.) It is evident that the main contribution to the field-driven loss of small ions (hence to τ_E) is due to particles in the size range of roughly 200 - 2000 μm -- this result is typical, as has been emphasized by *Dye et al.* [2003] -- whereas nearly all of the radar reflectivity is due to particles larger than 1 mm.

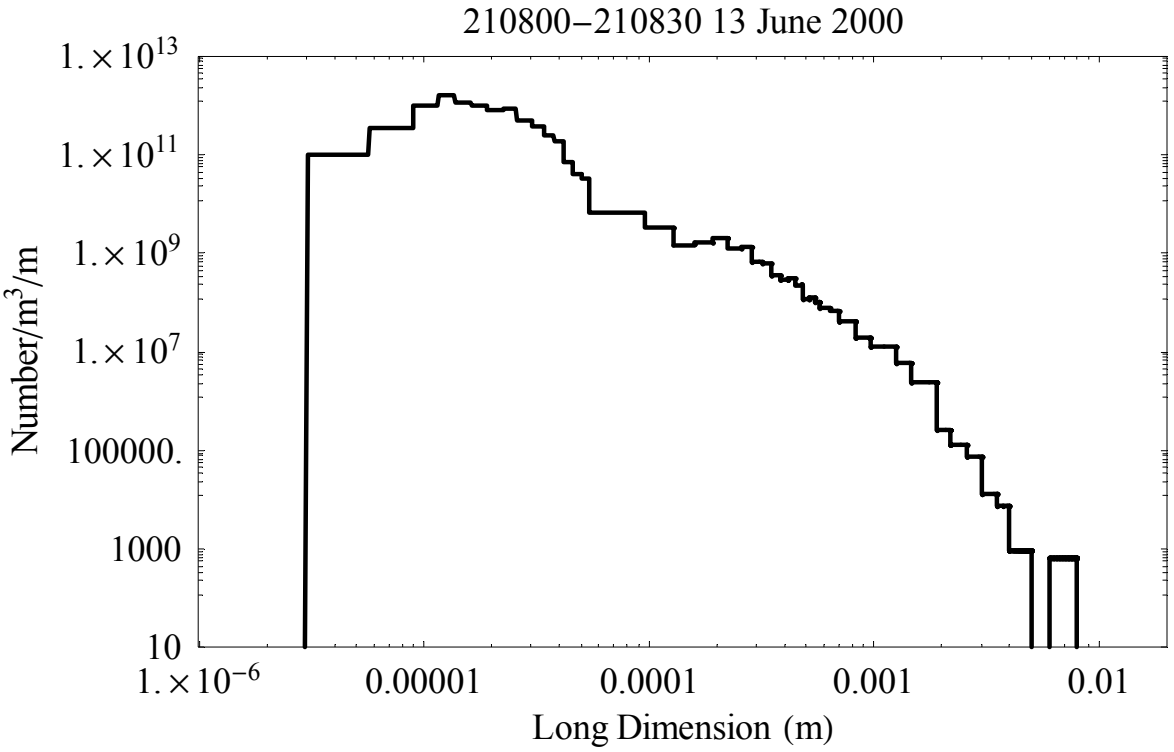

Figure 1 -- Composite particle-size spectrum for dense anvil from year 2000.

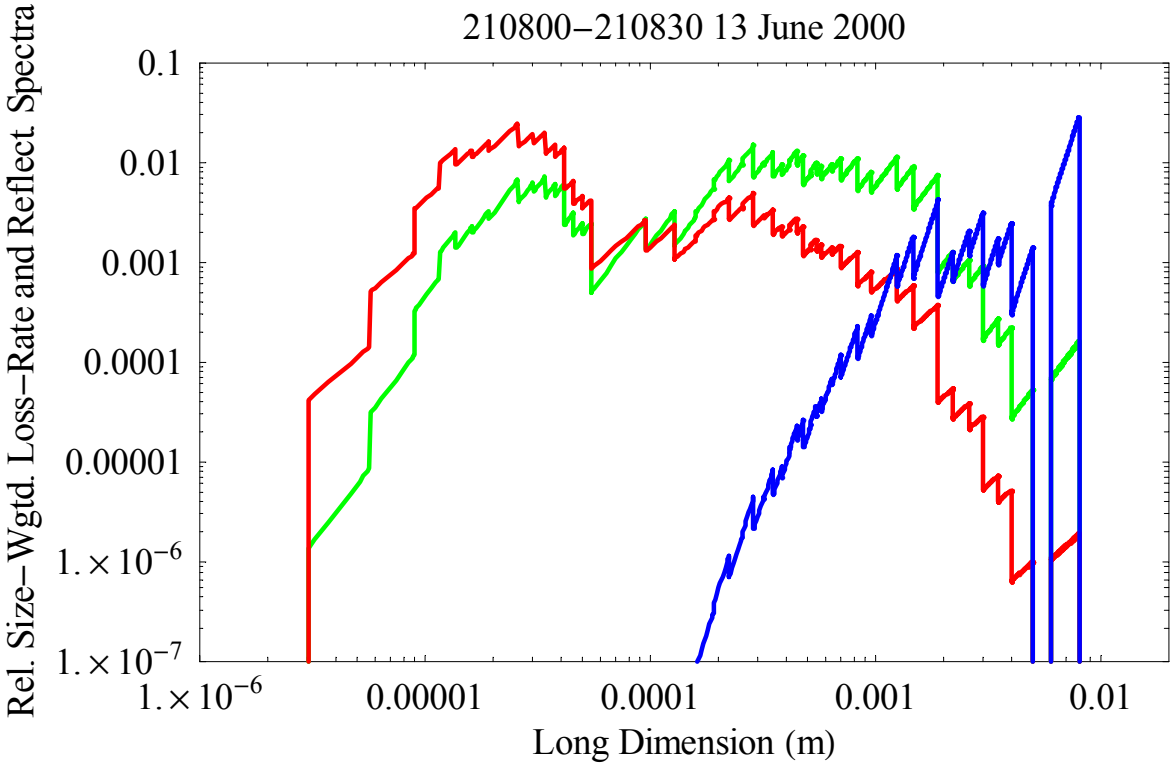

Figure 2 -- Relative spectra of diffusive-loss rate (red) and electrical-attachment-loss rate (green) of small ions and of radar reflectivity (blue) corresponding to the size distribution in Figure 1.

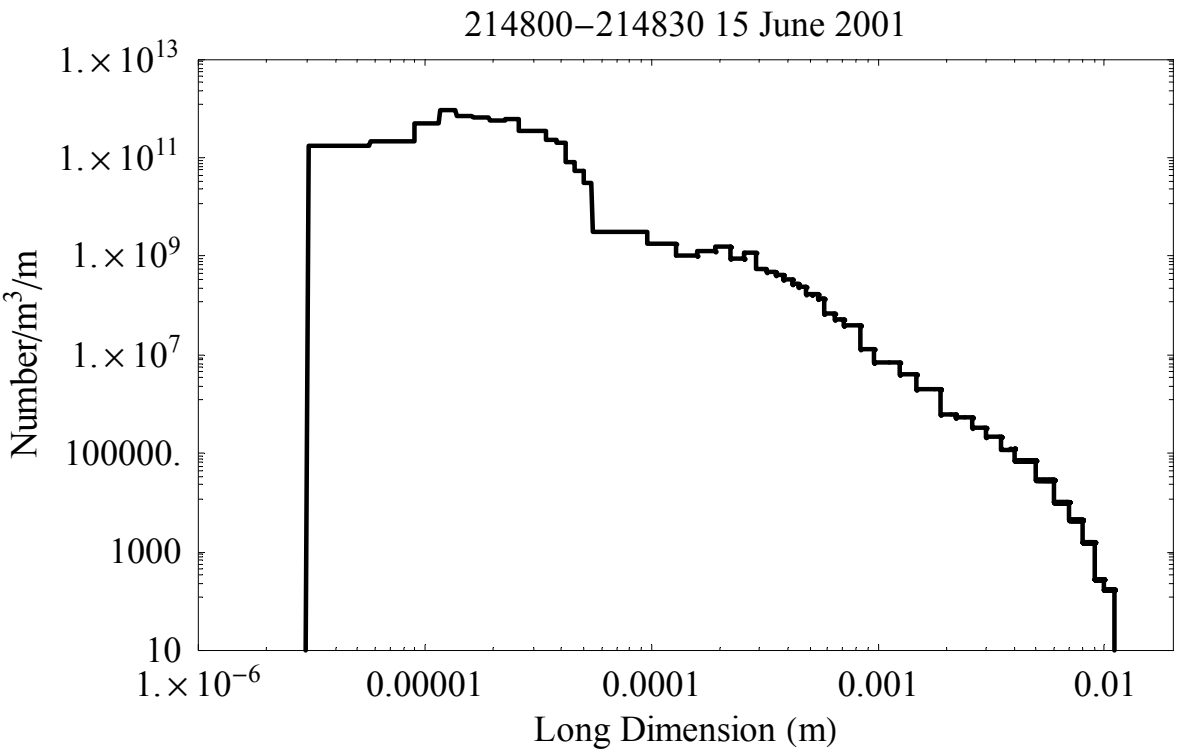

Figure 3 -- Composite particle-size spectrum for dense anvil from year 2001.

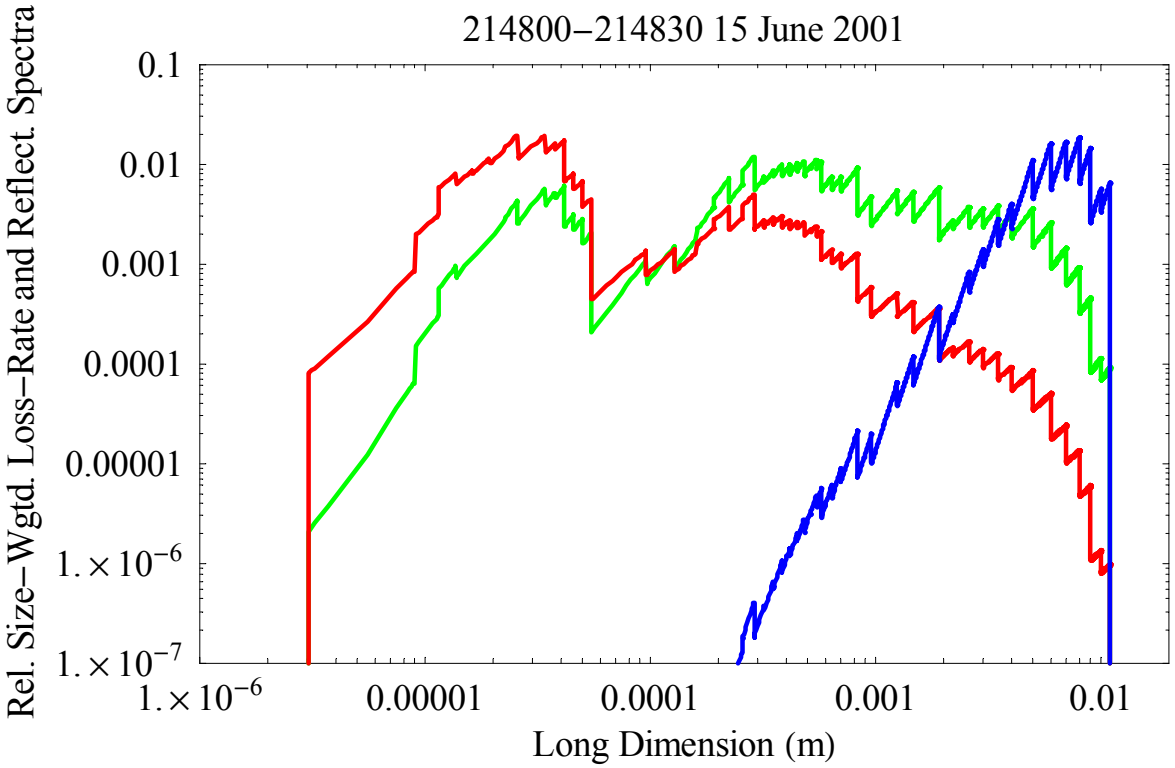

Figure 4 -- Similar to Figure 2 but corresponding to Figure 3.

Although the 210800-210830 (hhmmss UT) 13 June 2000 distribution is fairly broad, it is noisy at the largest sizes because the HVPS did not perform well during much of the year 2000 campaign. Therefore, similar results for 214800-214830 15 June 2001 at 8.6 km altitude are presented in Figures 3 and 4. (The model parameters for this case are τ_E = 7787 s, $E_.$ = 484 V/m, and τ_D = 75 s, for comparison with those of the former case.) The upper end of the size distribution here is seen to be both larger and better behaved than in the previous example, leading to a much clearer illustration that the radar reflectivity is dominated by only the very largest particles -- in this case those several mm in diameter -- which have little effect on the electrical decay time. Since τ_E and R_3.are dominated by distinct portions of the particle size distribution, one might expect these two parameters to be poorly correlated.

Starting with the "minflt" dataset, we first look at relationships between τ_E and the five partial particle concentrations listed above. For each of these it was necessary to filter out the same 79 cases, for which all partial concentrations = "NaN" -- an artifact of the microphysics processing at NCAR. For $N_{3\text{-}55}$ an additional 79 cases where that parameter equaled zero were filtered out, whereas for $N'_{>1000}$ it was necessary to filter out an additional 251 cases for which $N'_{>1000}$ = 0 although $N_{>1000}$ > 0. (This latter combination should not occur, and nearly all such cases were from year 2000.) The results are shown in Figures 5 - 10 below as scattergrams of τ_E vs. each partial concentration. In each case, the regression line is plotted in red and the number of samples and correlation coefficient are tabulated on the graph. (In Figure 10 and its statistics, two additional samples having very large values of $N'_{>1000}$ have been omitted. The correlation here is improved somewhat -- to 0.75 on 1477 samples -- without significantly changing the character of the scattergram if the additional 381 points from year 2000 are deleted.)

Evidently, both the "cleanest" scattergram and the maximum correlation coefficient in this group occur for τ_E vs. $N_{200\text{-}1000}$ (Figure 7), in agreement with the above discussion. The fact that the correlation coefficient does not decrease rapidly away from this maximum is an indication that the different size ranges in the particle spectrum tend to be fairly strongly correlated across all anvil cases, as observed previously by *Dye et al.* [2003].

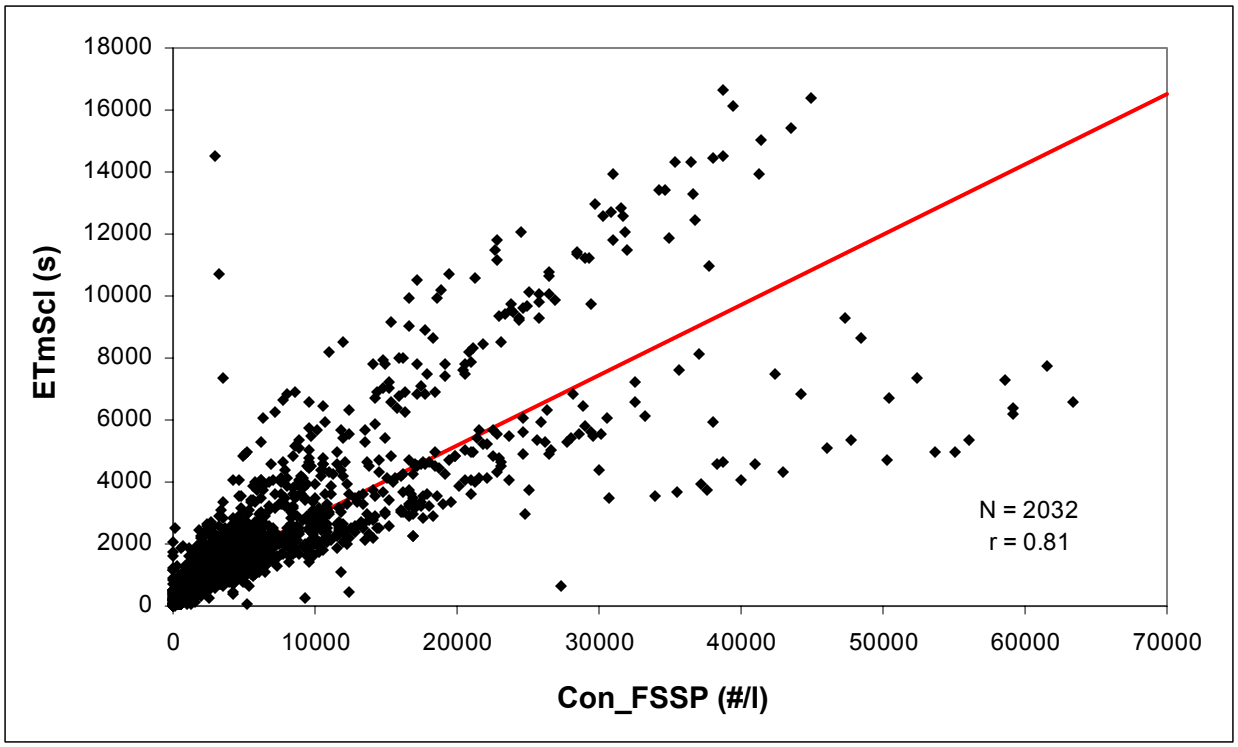

Figure 5 -- Scattergram of r_E vs. $N_{3\text{-}55}$ for all possible 30-s samples in the "minflt" dataset. The regression line is shown in red and the number of samples and correlation coefficient are listed.

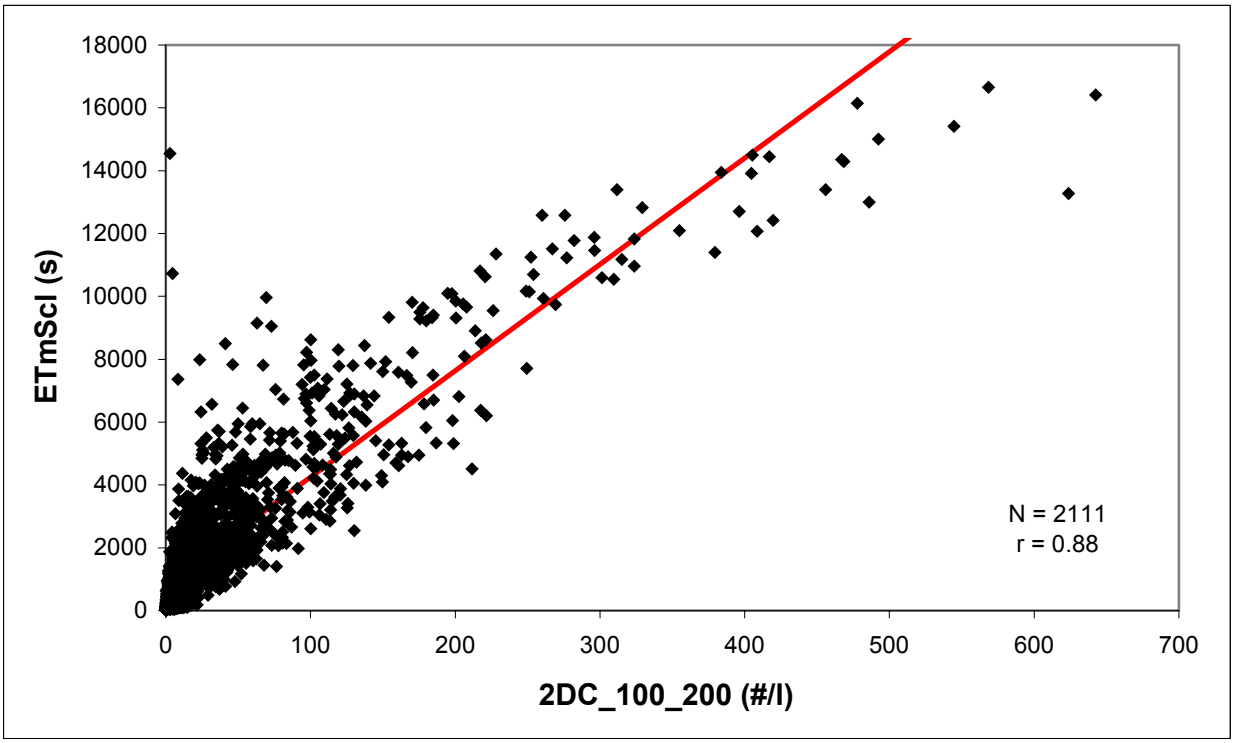

Figure 6 -- As in Figure 5 except for $N_{100\text{-}200}$.

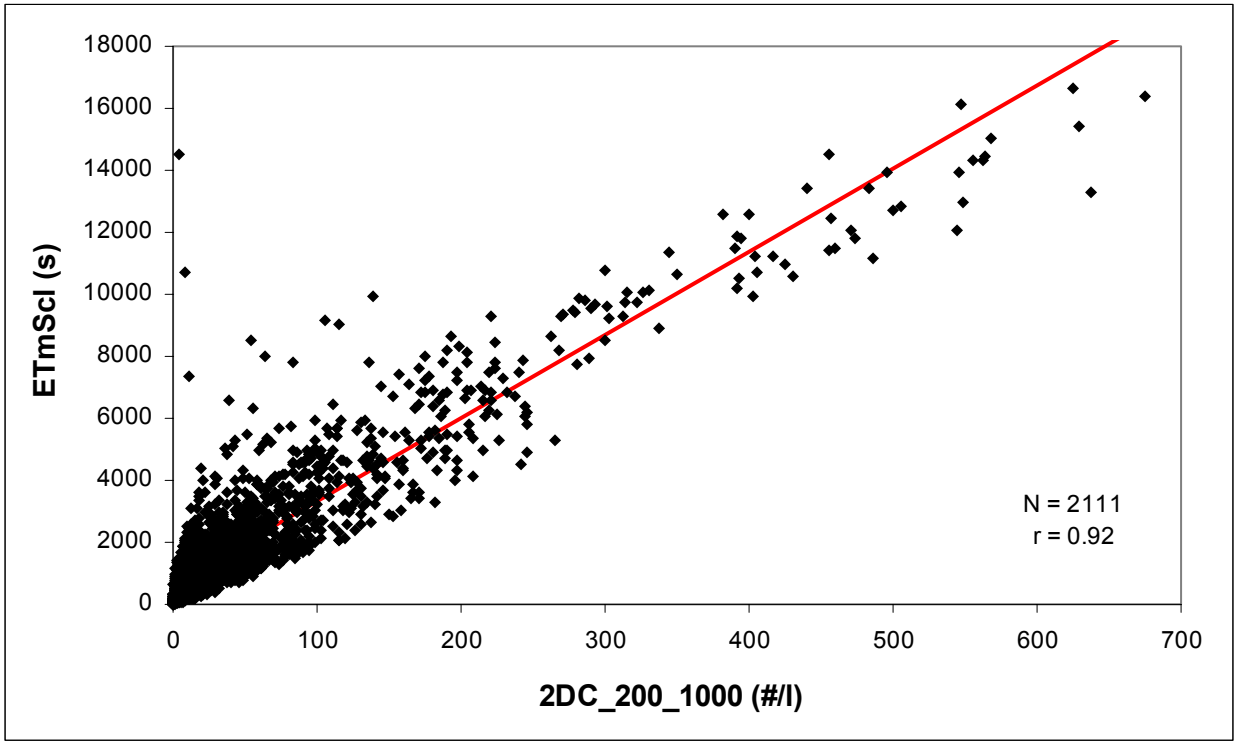

Figure 7 -- As in Figure 5 except for $N_{200\text{-}1000}$.

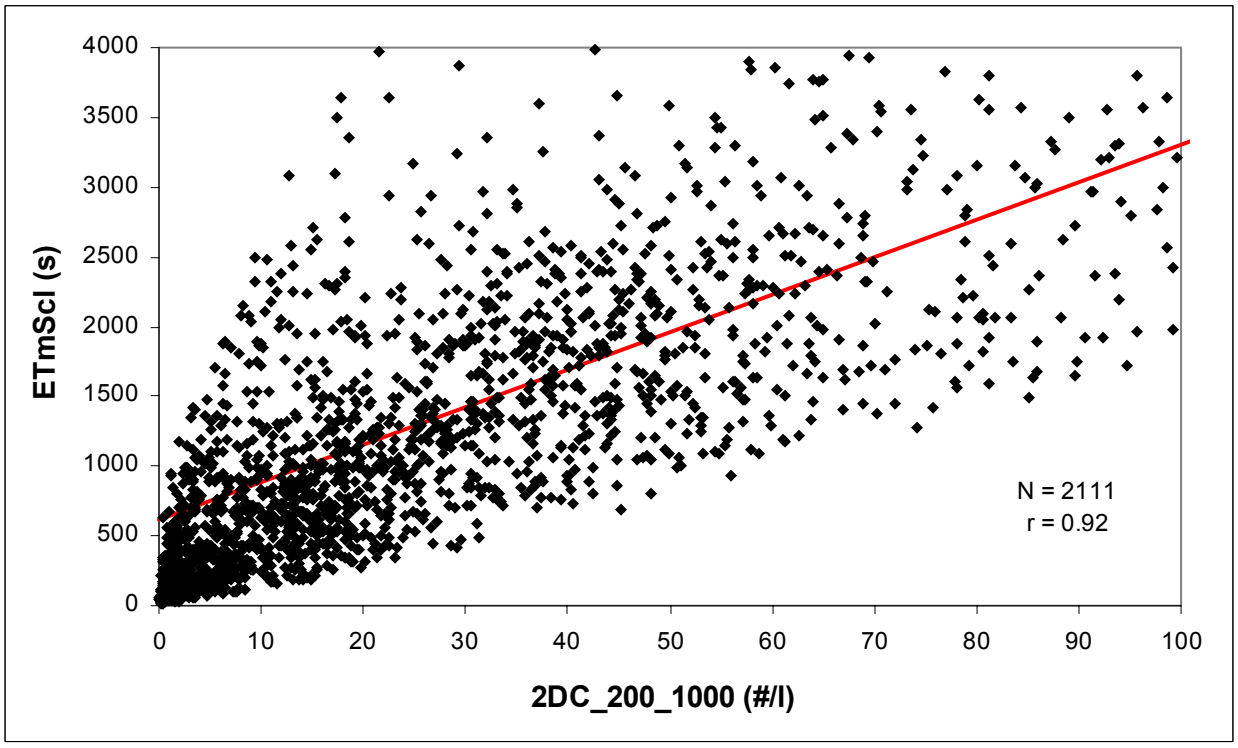

Figure 8 -- Magnification of the lower-left quadrant of Figure 7.

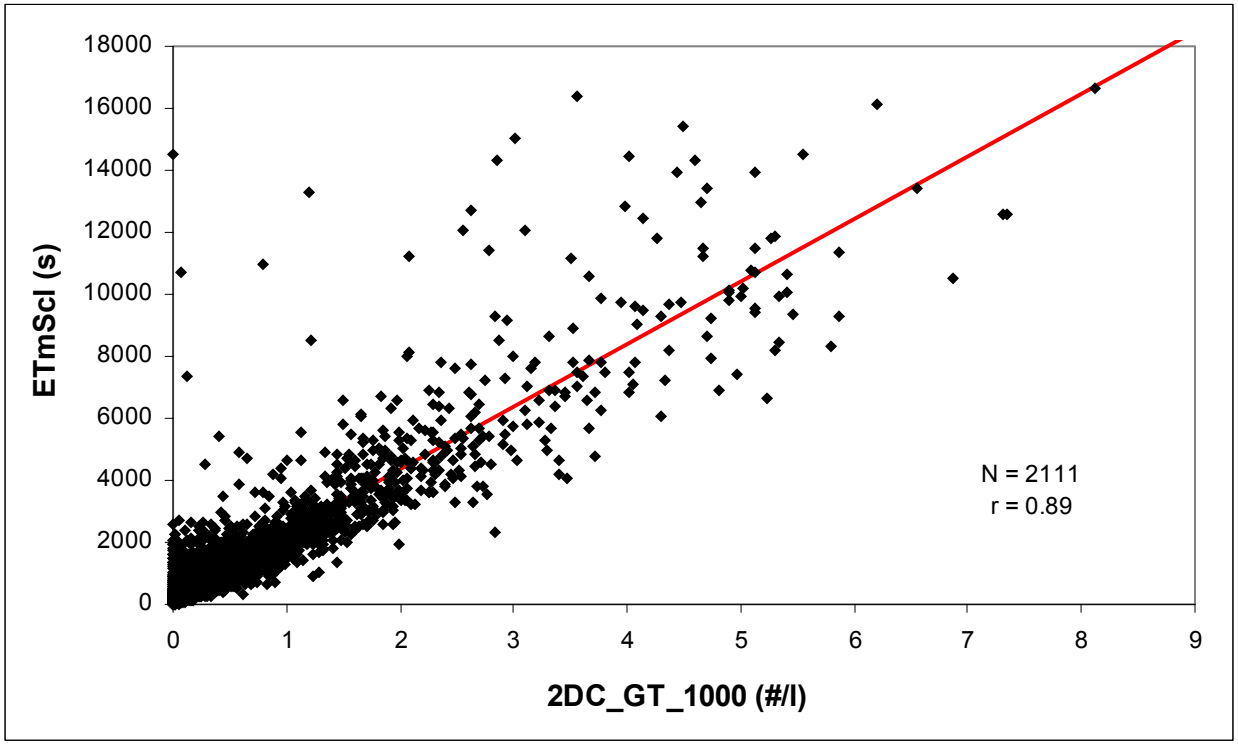

Figure 9 -- As in Figure 5 except for $N_{>1000}$.

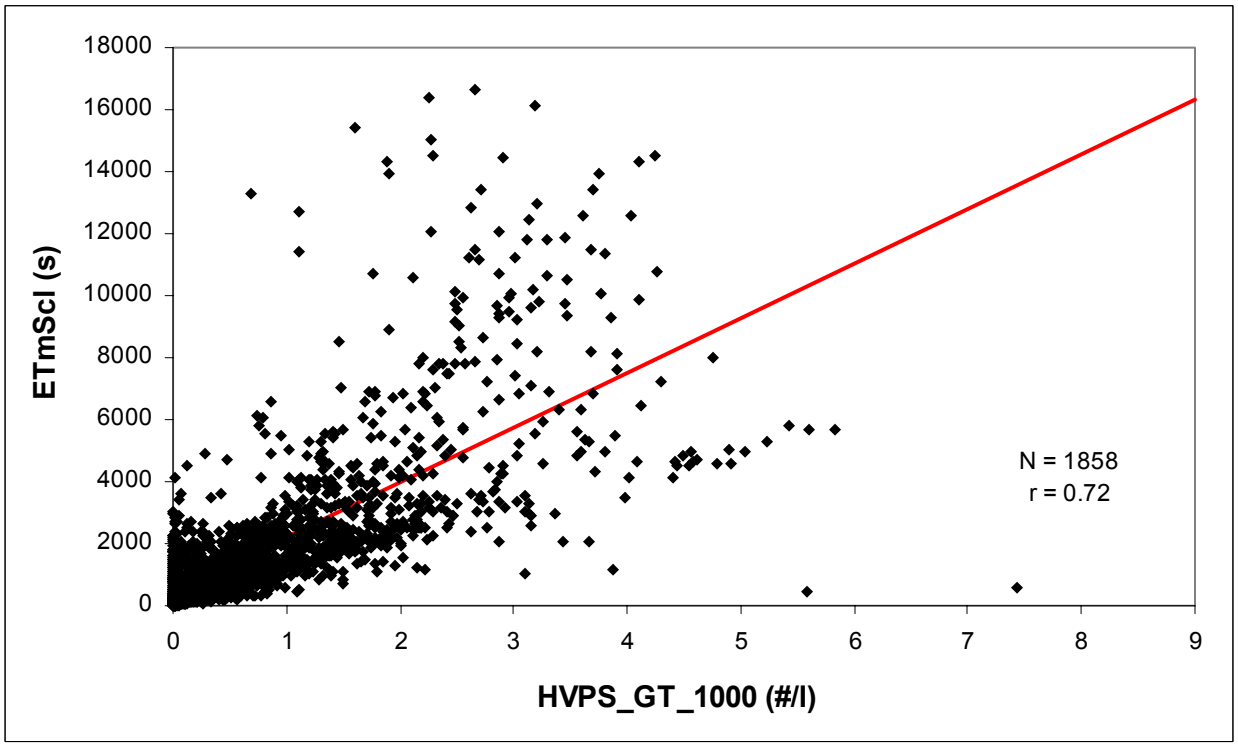

Figure 10 -- As in Figure 5 except for $N'_{>1000}$.

Next we look at relationships between R_3 and the particle distribution. Starting with the "minflt" dataset, samples for which the aircraft was in the cone of silence of the relevant radar (depending on whether or not NEXRAD data had been substituted for WSR-74C), and cells for which R_3 = "NaN," were deleted. In order to minimize the effects of statistical fluctuations and of scan gaps on R_3, we also deleted all points for which the number of 1 km^3 cells in the 27 km^3 average that contained radar data (NUMCUBE3X3) < 16. This left 1771 samples in the "radflt" dataset. It was then necessary to filter out the remaining 66 cases for which all partial concentrations = "NaN." Since it makes most sense to plot R_3 (dBZ) against the logarithm of the partial particle concentrations, an additional 32 cases where $N_{>1000}$ = 0 were filtered out, whereas for $N'_{>1000}$ it was necessary to filter out an additional 227 cases for which that parameter equaled zero. The results are shown in Figures 11 - 13 below.

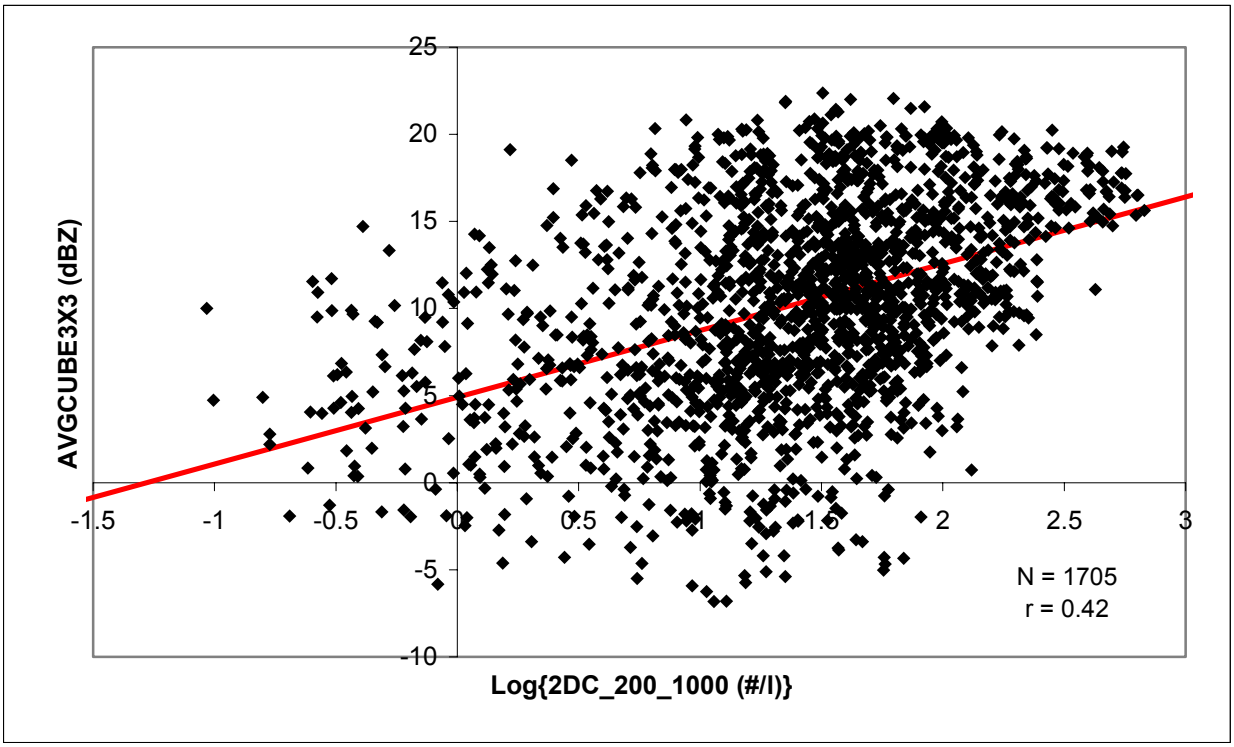

Figure 11 -- Scattergram of R_3 vs. log($N_{200\text{-}1000}$) for all possible 30-s samples in the "radflt" dataset. Otherwise similar to Figure 5.

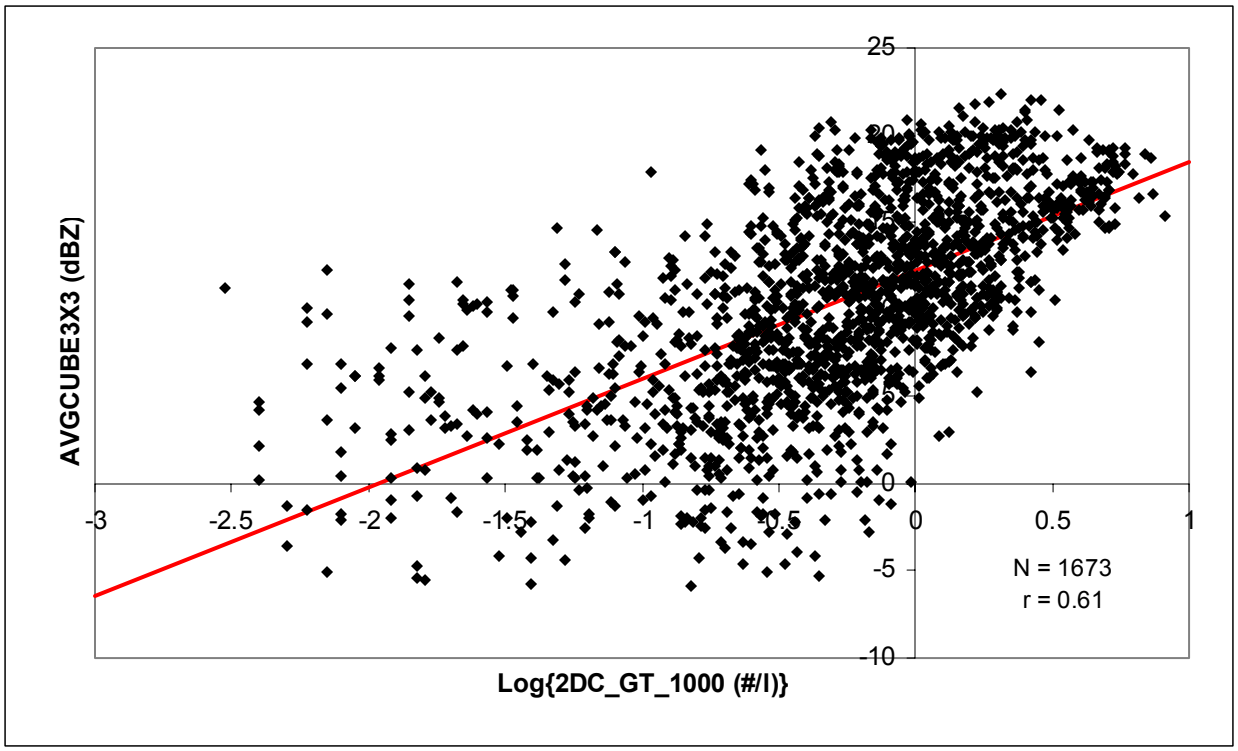

Figure 12 -- As in Figure 11 except for $N_{>1000}$.

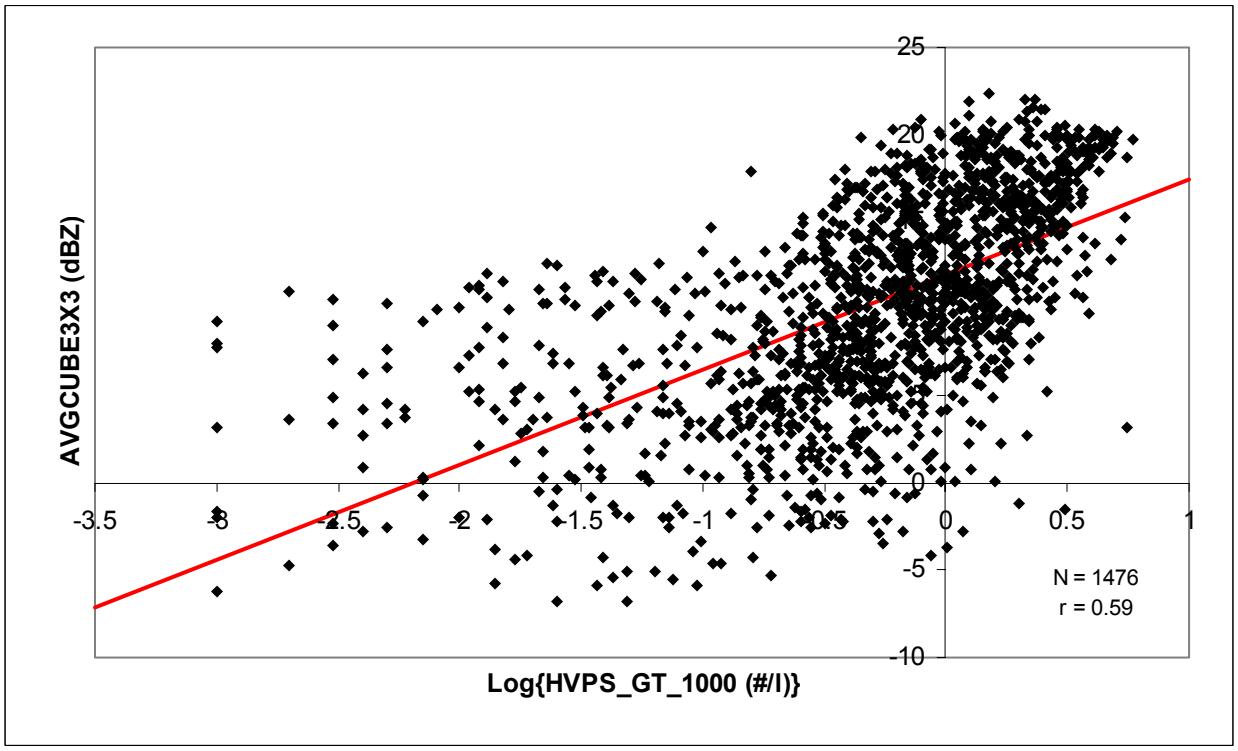

Figure 13 -- As in Figure 11 except for $N'_{>1000}$.

(In Figure 13 and its statistics, the same two samples having very large values of $N'_{>1000}$ have been omitted. The correlation here is improved somewhat -- to 0.63 on 1206 samples -- without significantly changing the character of the scattergram if the additional 270 points from year 2000 are deleted.)

Evidently the above discussion is again corroborated. We find that radar reflectivity is much better correlated with $N_{>1000}$ (or with $N'_{>1000}$) than with $N_{200\text{-}1000}$. (That the former correlations are not better still can probably be explained by the obvious fact that 30 s of aircraft track -- roughly 3.5 km -- samples a much smaller volume of cloud than a 27 km^3 radar average.) Thus, it is somewhat surprising that the relationship between R_3 (logarithm of the integral of d^6 over the size distribution) and the logarithm of τ_E (proportional to the integral of d^2) is as good as it is (see Figure 14).

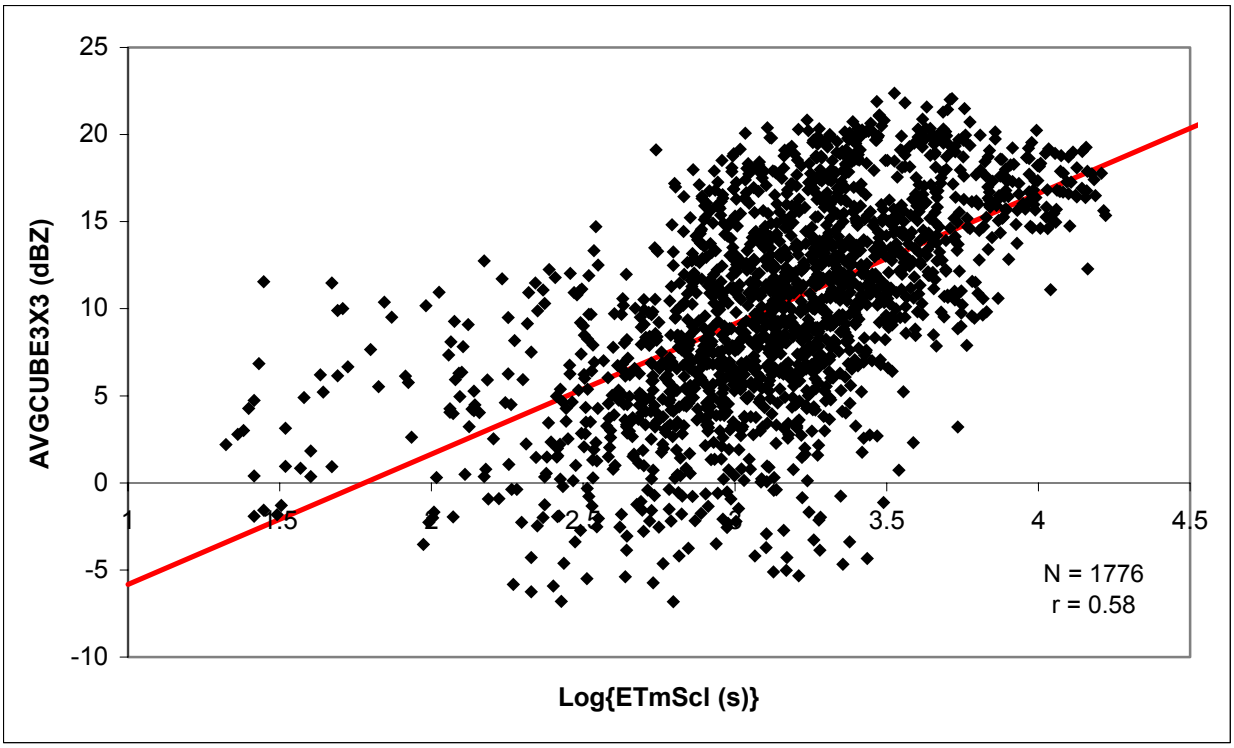

Figure 14 -- Scattergram of R_3 vs. log(τ_E) for all possible 30-s samples in the "radflt" dataset (including the 5 cases with $|\boldsymbol{E}|$ = "NaN"). Otherwise similar to Figure 5.

Dependence of τ_E on $|\boldsymbol{E}|$

Of most interest here, of course, is the relationship between τ_E and $|\boldsymbol{E}|$. Figures 15 and 16 show this for the "minflt" dataset. Evidently there is a moderately good correlation between these parameters.

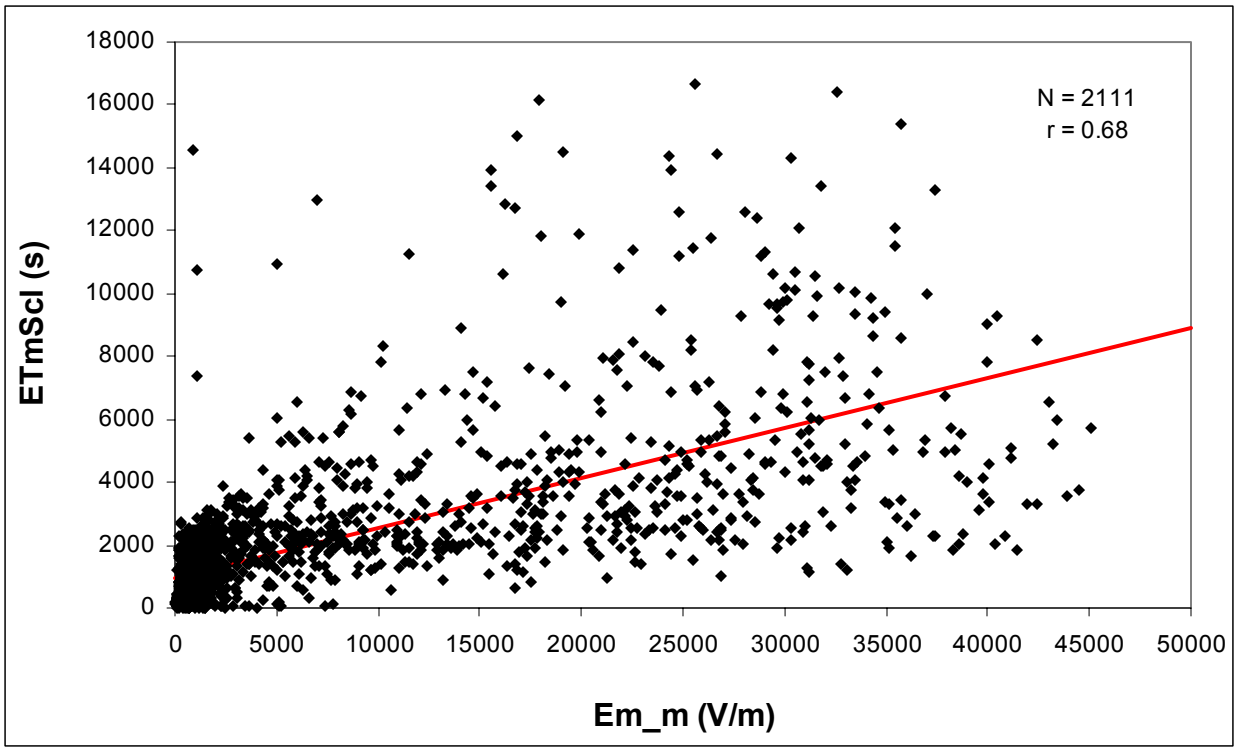

Figure 15 -- Scattergram of τ_g vs. $|E|$ for the "minflt" dataset. Otherwise similar to Figure 5.

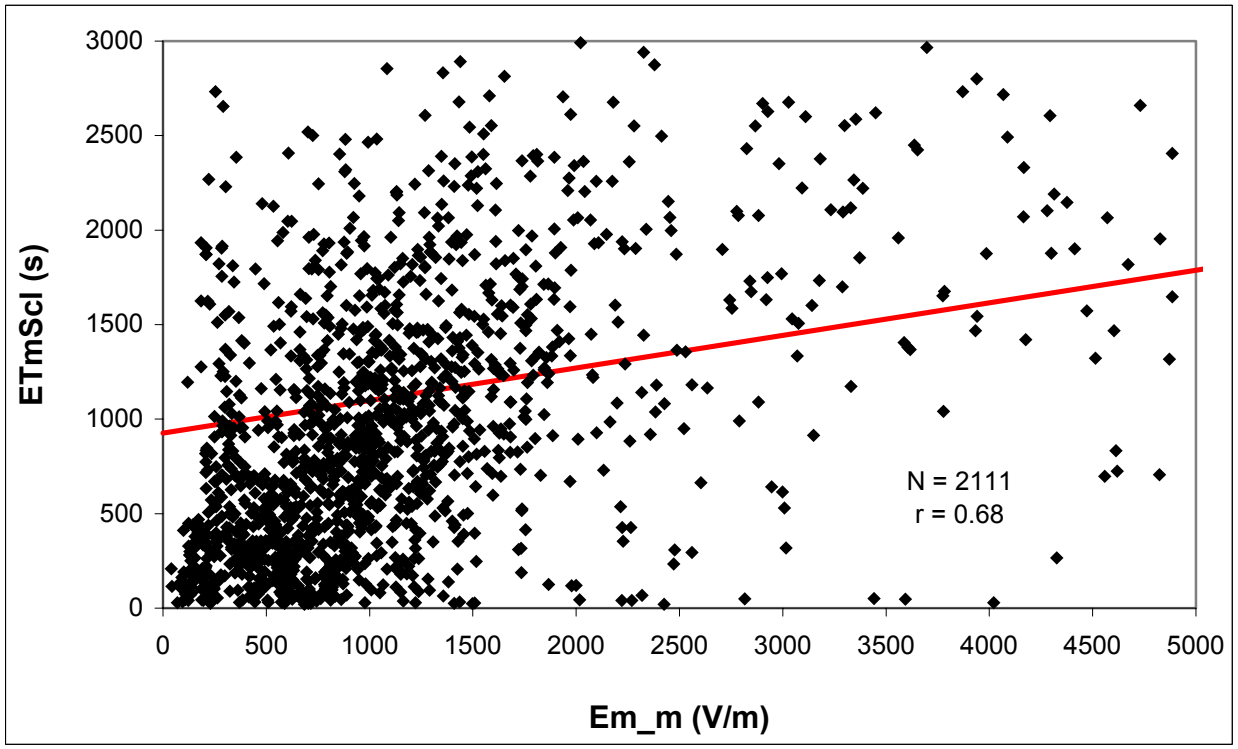

Figure 16 -- Magnification of the lower-left quadrant of Figure 15.

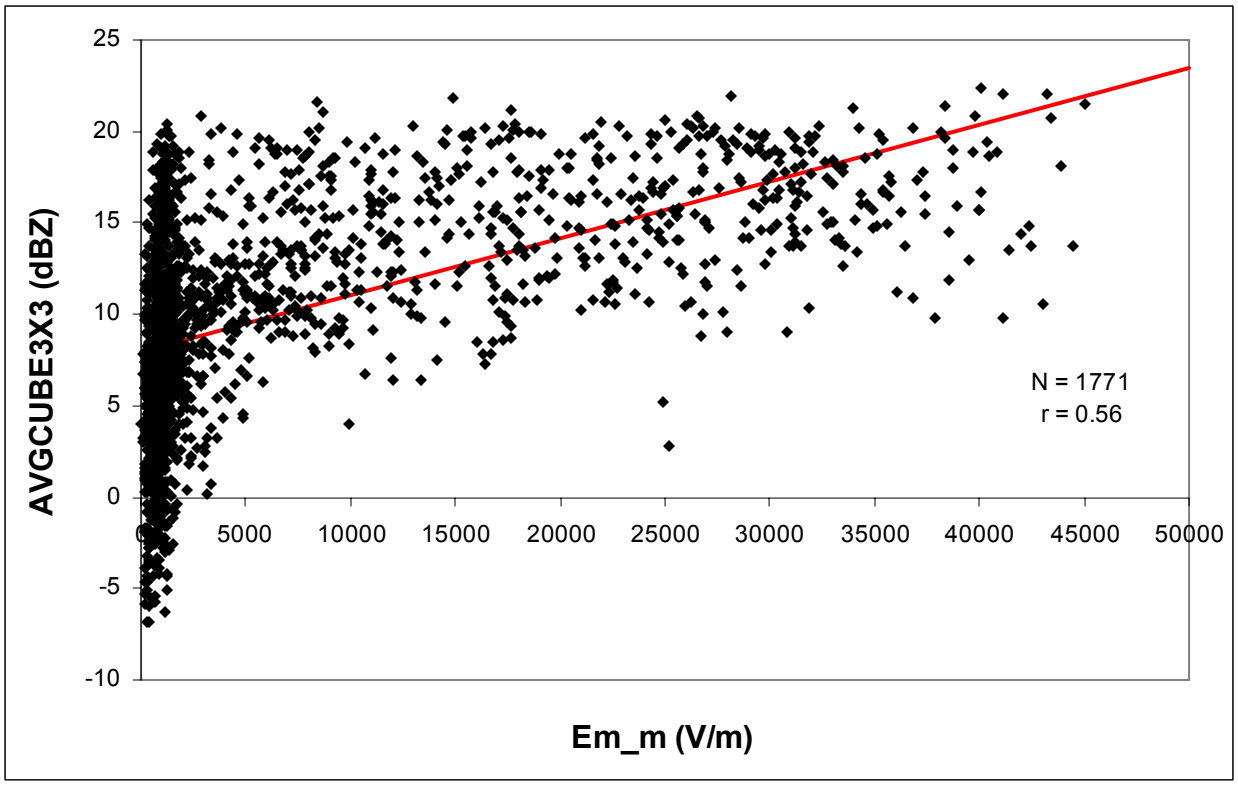

Figure 17 -- Similar to Figure 11 for R_3.

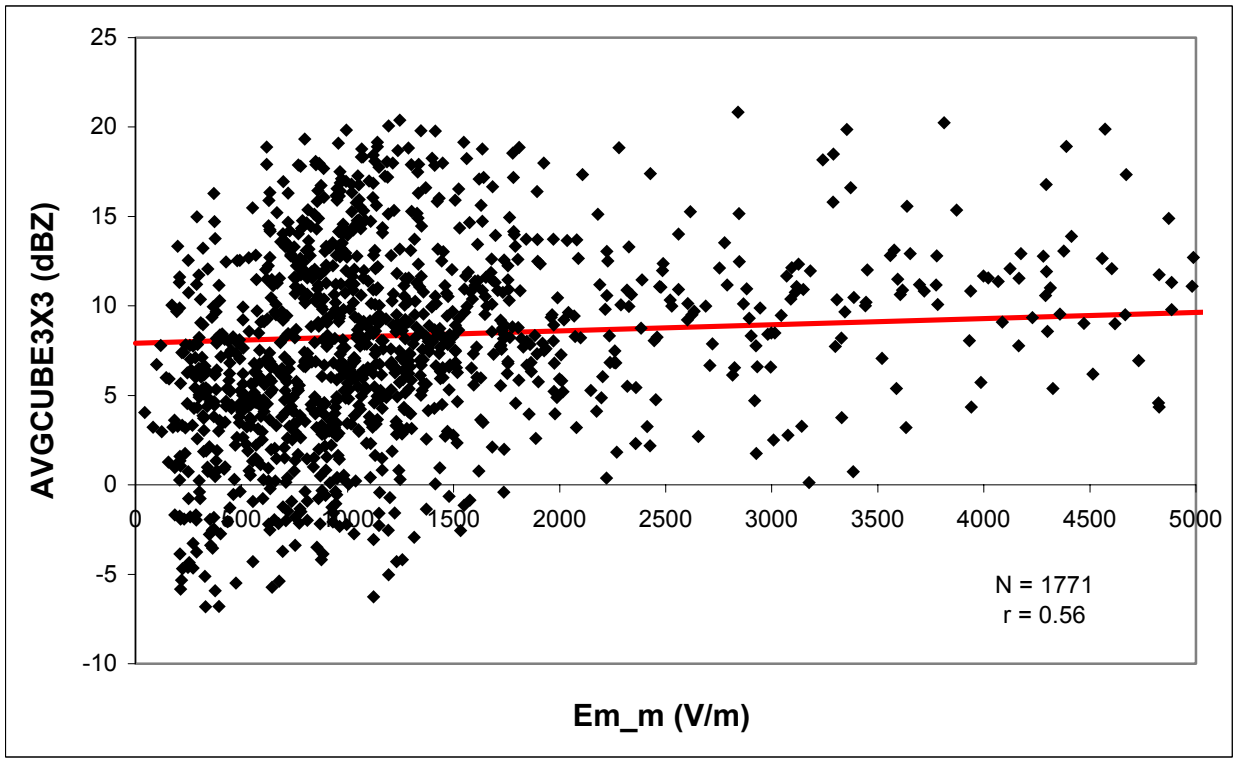

Figure 18 -- Magnification of the left side of Figure 17.

It is clear that most cases with low τ_E (say, τ_E < 1000 s) also have low |$\boldsymbol{E}$|, whereas most cases with high τ_E (say, τ_E > 3000 s) have moderate to high |$\boldsymbol{E}$|. The problem is that, for intermediate τ_E, |$\boldsymbol{E}$| can apparently take on any value. This distribution is like the "threshold" behavior of R_3 (and other radar averages) vs. |$\boldsymbol{E}$|, illustrated in Figures 17 and 18 for the "radflt" dataset, where there are very few cases with |$\boldsymbol{E}$| > 5 kV/m for R_3 < 6 dBZ.

To illustrate the thresholding of τ_E vs. |$\boldsymbol{E}$| in more detail, the table on p.15 lists all cases in the "minflt" dataset having both τ_E < 1000 s and |$\boldsymbol{E}$| > 2 kV/m. We term these cases "violators," in the sense that they might be inferred to violate the model prediction that high fields cannot be sustained by anvil clouds with low electrical-decay time scales. Such cases may not actually violate the model, however; in an electrified cloud there should always be some parcels in the process of field decay, no matter how short their τ_E. There are only 53 such cases out of 2111 samples in the dataset, 29 of which have |$\boldsymbol{E}$| > 3 kV/m. Notice that many of these violators have various NCAR "filter flags" set. For example, 19 have "Anvil_Type" < 8, which means that the anvil has either low-level radar returns beneath a well-defined base (which might signify precipitation) or a base lower than 5 km (the nominal freezing level). Fifteen cases have "core_20km" = 1, which means that the aircraft was within 20 km of a convective core having radar reflectivity greater than 40 dBZ at 4 km altitude (hence, the measured field might be due to non-local charge within the core). Ten have "LDARm5" > 2, meaning that there were LDAR sources within 20 km during the previous 5 min. Finally, three cases had "CGm5" ≥ 1, meaning that a C/G strike point was similarly located by the CGLSS. (In these last two groups, lightning might have deposited the charge giving rise to the measured field.) If we throw out all of the above flagged cases, there remain only 22 violators, 11 of which have |$\boldsymbol{E}$| > 3 kV/m.

Applying these four filters to the "minflt" dataset results in the "cldltgflt" dataset, improving the correlation between τ_E and |$\boldsymbol{E}$| somewhat -- to 0.75 on 1090 samples. (Note, however, that the lightning filters used here are not perfect, since one or both of the lightning-detection systems were not working properly during portions of several anvil flights. I have not attempted to remove such cases from the present analysis.) Notice that the number of violators over both |$\boldsymbol{E}$| thresholds has decreased substantially more than the number of samples in going from the "minflt" to the "cldltgflt" dataset, making this distribution (see Figures 19 and 20) our best statistical representation of the performance of the electrical-decay model.

Date	Time	z	|E|	Top	Base	R3	LDARm5	CGm5	ETmScl	Anvil_Type	core_20km
yy/mm/dd	hhmmss	m	V/m	km	km	dBZ	#	#	s	code	code
00/06/04	213830	7996	6631	11.8	5.2	10.8	NaN	0	302	10	0
00/06/04	215500	7354	7688	10.2	4.2	18.5	NaN	0	907	4	0
00/06/04	215530	7354	10641	9.5	4.5	19.1	NaN	0	549	4	0
00/06/04	215700	7172	2561	9.7	5.1	10.9	NaN	0	295	4	0
00/06/04	215900	6768	2265	10.6	7.0	6.8	NaN	0	426	10	1
00/06/04	221500	5130	5103	9.3	4.9	10.9	NaN	0	209	4	0
00/06/04	221530	5068	3442	9.2	5.0	10.0	NaN	0	51	10	0
00/06/04	221630	5071	6734	9.5	4.2	13.5	NaN	0	983	10	0
00/06/13	212000	11202	4613	10.9	7.4	10.6	0	0	833	10	0
00/06/13	212700	11200	13193	11.2	3.9	10.0	6	0	891	10	1
00/06/13	213400	11209	17497	10.3	5.5	13.0	2	0	805	10	1
00/06/13	213700	11194	2133	10.4	6.0	8.1	0	0	729	10	0
00/06/13	214400	11211	2604	11.2	7.6	10.1	6	0	663	10	1
00/06/13	215000	11206	16743	10.4	4.4	7.8	0	0	651	10	1
00/06/13	215800	11203	2946	10.7	6.8	9.9	2	0	641	10	1
00/06/13	220330	11202	4618	10.2	4.3	9.0	0	0	724	10	0
00/06/13	221200	11201	2009	10.5	4.2	5.8	0	0	894	10	0
00/06/13	222400	11209	2215	10.4	3.0	9.8	0	0	536	4	0
00/06/13	222430	11203	2222	10.2	3.1	10.6	0	0	427	4	0
00/06/13	222500	11200	2099	10.1	3.4	8.2	0	0	927	4	0
00/06/13	225130	9306	26902	10.0	3.0	15.1	0	0	993	4	0
00/06/13	225500	9305	21228	9.9	3.0	13.1	0	0	964	4	0
00/06/14	225030	9353	5032	12.9	3.1	10.9	12	0	106	4	1
00/06/14	225100	9354	7800	13.9	3.3	12.8	8	0	149	4	1
00/06/28	192630	9310	2360	8.9	5.2	5.4	0	0	919	10	0
00/06/28	194230	8033	3008	7.9	4.9	2.5	0	0	530	10	0
00/06/28	194830	8035	2260	8.6	5.0	7.5	0	2	884	10	0
01/05/25	190200	6020	7412	11.5	4.2	9.9	25	0	49	4	1
01/05/25	190230	6021	5096	11.9	4.7	6.7	8	0	53	4	1
01/05/25	190830	6037	2016	11.5	4.9	5.2	0	0	44	10	0
01/05/25	190900	6033	5170	11.6	4.3	7.7	0	0	63	10	0
01/05/25	190930	6036	2319	11.2	4.5	5.5	0	0	67	4	0
01/05/25	191000	6040	2221	11.1	5.4	0.4	0	0	40	4	0
01/05/25	191030	6035	2269	11.5	5.5	1.8	0	0	40	4	0
01/05/25	191100	6032	2426	11.9	5.6	2.2	0	0	21	10	0
01/05/25	191400	6033	2815	11.2	4.9	6.1	0	0	49	10	0
01/05/25	191600	6032	2227	9.5	5.3	12.5	0	0	354	10	0
01/05/25	191630	6022	2998	8.2	4.7	8.5	0	0	615	10	0
01/05/25	210530	6678	2164	9.0	5.1	11.7	4	0	986	10	0
01/05/28	202500	9226	4559	9.4	5.4	12.7	0	0	697	6	1
01/05/28	202530	9226	2472	9.3	4.4	11.1	0	0	233	6	1
01/05/29	202730	9250	4824	11.4	5.8	4.6	7720	15	706	10	1
01/06/04	190600	5405	4326	7.4	4.2	5.4	9	0	266	10	0
01/06/04	201130	9273	3594	14.4	5.0	11.5	92	0	47	10	1
01/06/04	202330	9270	3149	13.0	7.3	10.9	1	0	915	10	0
01/06/04	202430	9266	6285	12.3	7.0	10.5	2	0	546	10	0
01/06/04	202500	9264	3015	11.9	6.6	8.5	2	0	319	10	0
01/06/04	202800	9588	6034	12.8	7.6	11.6	1	0	720	10	0
01/06/04	204500	9895	2790	13.1	8.2	11.2	0	0	990	10	0
01/06/04	205230	9891	2477	12.9	9.3	11.0	0	0	308	10	0
01/06/04	205330	9891	2521	12.8	7.7	10.3	0	0	949	10	0
01/06/24	181530	6955	4021	11.3	5.5	11.6	0	32	28	10	1
01/06/24	195900	5675	7861	11.5	3.9	9.9	0	0	872	4	0

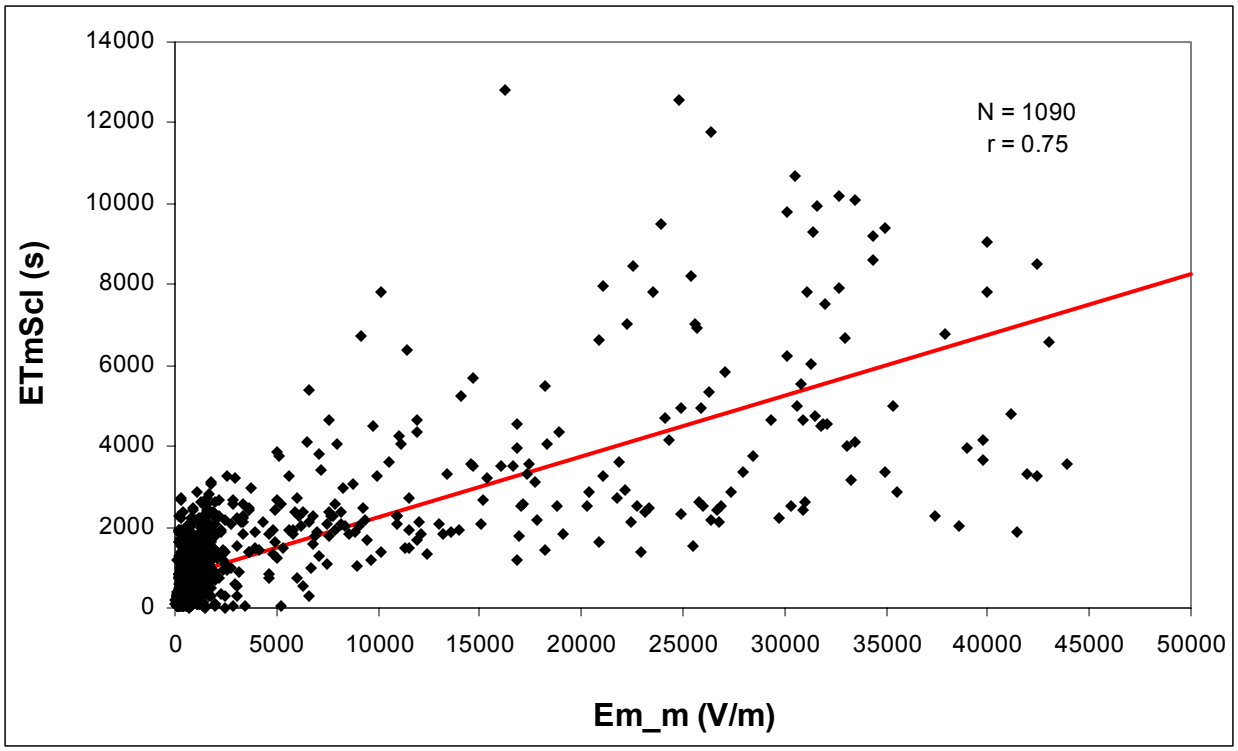

Figure 19 -- Scattergram of τ_E vs. $|E|$ for all 30-s samples in the "cldltgflt" dataset. Otherwise similar to Figure 5.

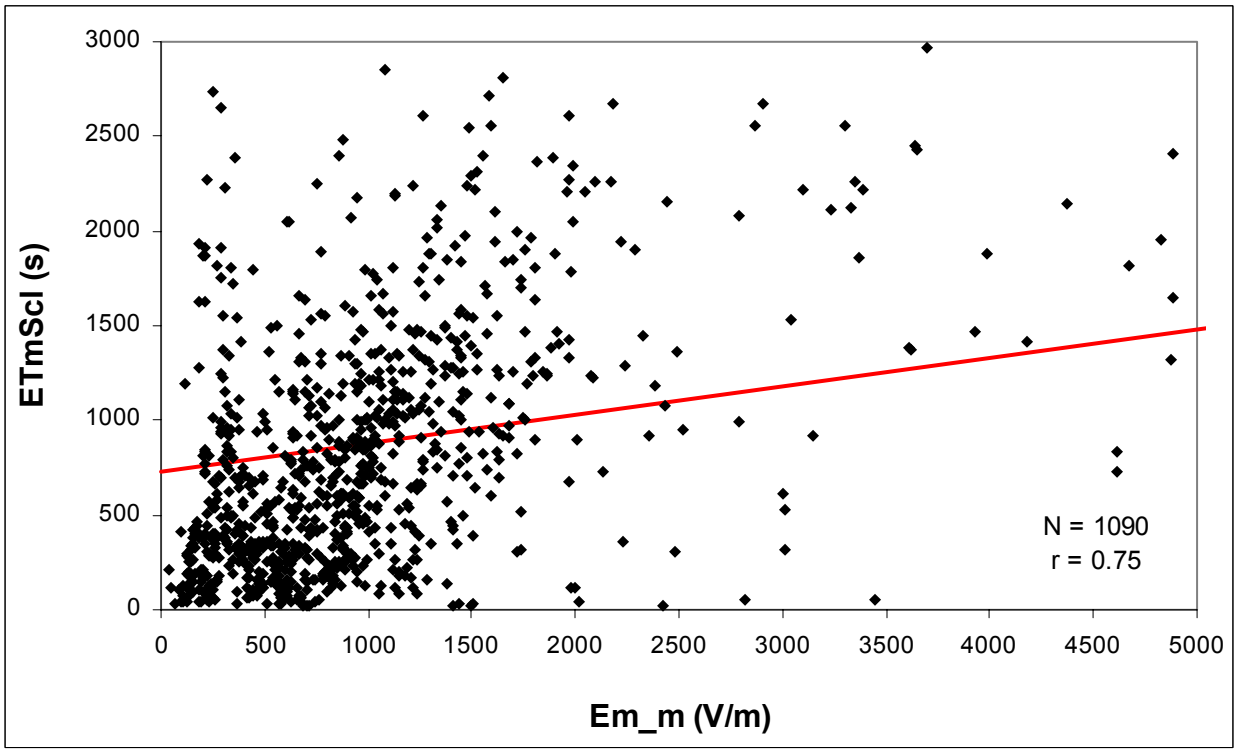

Figure 20 -- Magnification of the lower-left quadrant of Figure 19.

(The character of these scattergrams is not much different, however, from those shown in Figures 15 and 16.)

Since we are attempting to validate the electrical-decay model with this analysis, it makes sense to check for comparable relationships between $|\boldsymbol{E}|$ and other cloud-physical parameters besides τ_E. Figures 21 - 23 display scattergrams of $N_{100\text{-}200}$, $N_{200\text{-}1000}$, and $N_{>1000}$ vs. $|\boldsymbol{E}|$ on the "cldltgflt" dataset. Although there is no suggestion of "thresholding" in any of these plots (in contrast to Figure 19) it must be admitted that the correlation coefficient of $|\boldsymbol{E}|$ with $N_{>1000}$ is just as good as that with τ_E.

Examination of the radar "curtains" in the "MER" files on the NCAR Web site indicates that the aircraft was sometimes flying well above or below the radar center of the anvil that it was investigating (note especially the flight on 000613). Hence, elevated fields due to charge in the interior of the cloud might not be expected to correspond to the local cloud-physical conditions (hence, to the computed value of τ_E). Two different automated filters were devised and applied to the "cldltgflt" dataset in an effort to select those cases when the aircraft was near the radar center of the cloud. Each filter was adjusted to remove about half of the samples. Neither filter significantly changed the character of the τ_E vs. $|\boldsymbol{E}|$ scattergram.

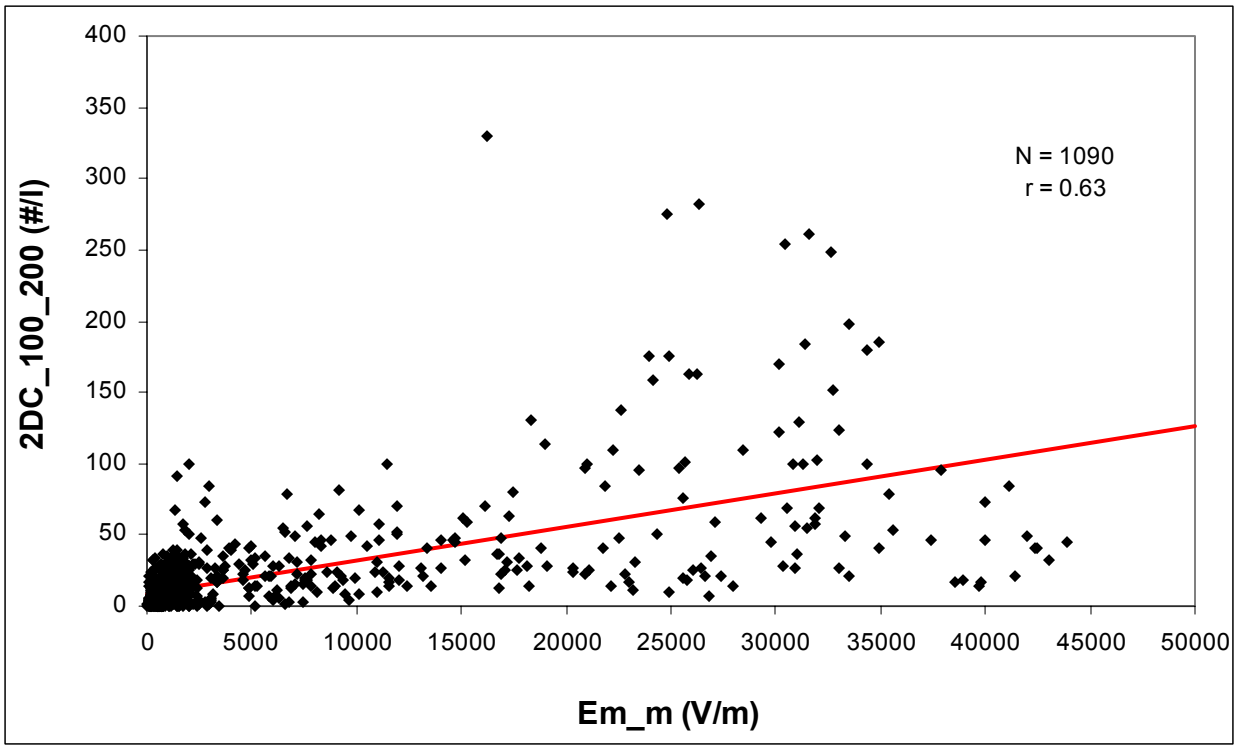

Figure 21 -- Scattergram of $N_{100\text{-}200}$ vs. $|E|$ for all 30-s samples in the "cldltgflt" dataset. Otherwise similar to Figure 5.

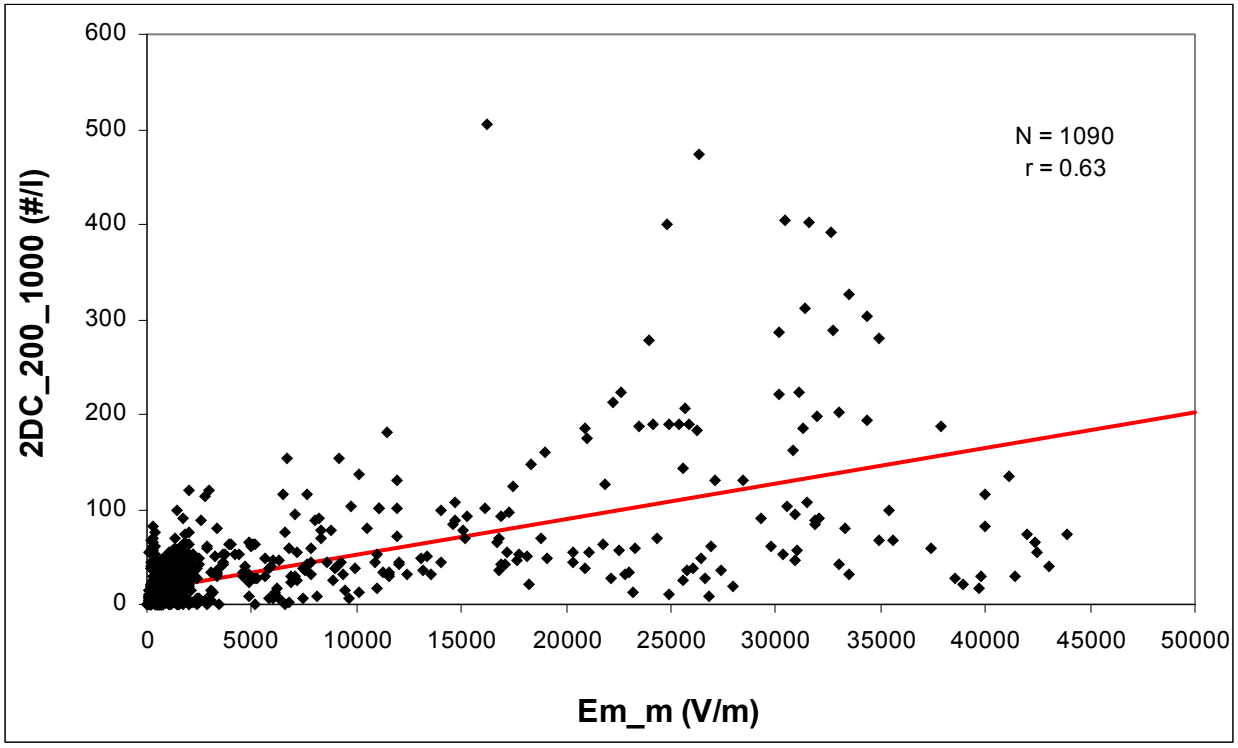

Figure 22 -- As in Figure 21 except for $N_{200-1000}$.

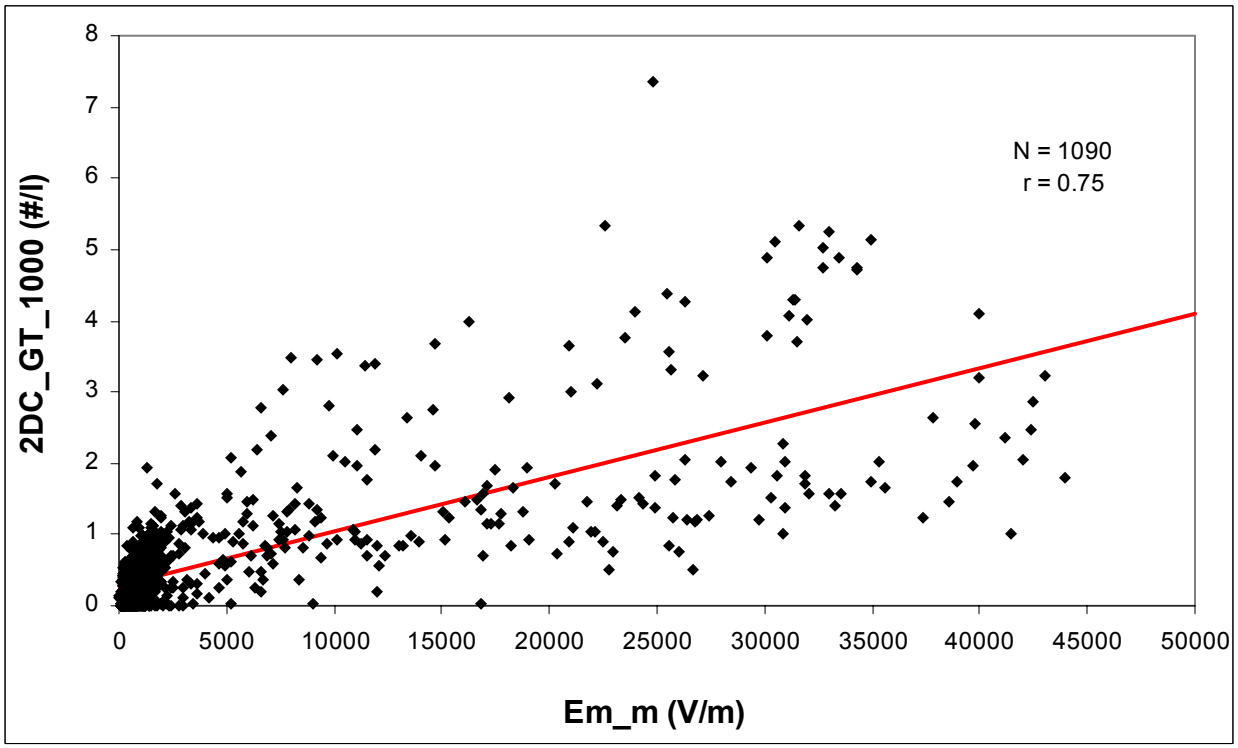

Figure 23 -- As in Figure 21 except for $N_{>1000}$.

The first of these filters was based on NUMCUBE3X3 and the corresponding standard deviation ("SDEVCUBE3X3") of reflectivity among the 1 km^3 cells making up the 27 km^3 average, R_3. We could require the reflectivity to be relatively constant near the aircraft by deleting cases with NUMCUBE3X3 < 18 or SDEVCUBE3X3 > 4 dBZ. This filter reduced the correlation between τ_E and $|\boldsymbol{E}|$ slightly -- to 0.72 on 557 samples. The number of violators was reduced less than the number of samples -- to 11 for $|\boldsymbol{E}|$ > 2 kV/m and to 6 for $|\boldsymbol{E}|$ > 3 kV/m. More than 3/4 of the samples from flight 000613 were deleted.

The second filter was more complex. We estimated the relative deviation of the aircraft altitude from the height of maximum reflectivity in the 11 X 11 km^2 column centered on the aircraft position using the expression,

ABS(POS_Alt/1000-ALT_MAX11X11)/((TOP11X11-BASE11X11)/2),

and we estimated the relative deviation from the center of the anvil with the formula,

ABS(POS_Alt/1000-(TOP11X11+BASE11X11)/2)/((TOP11X11-BASE11X11)/2),

where "ALT_MAX11X11" is the altitude of maximum reflectivity, "TOP11X11" is the average altitude of the top of the radar anvil in the 11 X 11 km^2 column centered on the aircraft position, and BASE11X11 is the average bottom of the anvil in the same column. When all samples were deleted for which either of these expressions was ≥ 0.75, the correlation between τ_E and $|\boldsymbol{E}|$ was unchanged -- 0.75 on 542 samples. The number of violators was reduced roughly in proportion to the number of samples -- to 8 for $|\boldsymbol{E}|$ > 2 kV/m and to only three for $|\boldsymbol{E}|$ > 3 kV/m. All of the samples from flight 000613 were deleted. Since this second filter appeared slightly more effective, the resulting scattergram is reproduced in Figures 24 and 25.

As demonstrated above, there is considerable, but not overwhelming, statistical evidence in favor of the electrical-decay model. τ_E vs. $|\boldsymbol{E}|$ exhibits similar thresholding behavior to R_3 vs. $|\boldsymbol{E}|$ but with a larger correlation coefficient. (The correlation between R_3 and Log$|\boldsymbol{E}|$ is higher but still doesn't win out.) Both the correlation and the thresholding can be improved by physically justifiable filtering. On the other hand, the correlation between $N_{>1000}$ and $|\boldsymbol{E}|$ is just as high (although with no thresholding behavior) as that between τ_E and $|\boldsymbol{E}|$ on the "cldltgflt" dataset.

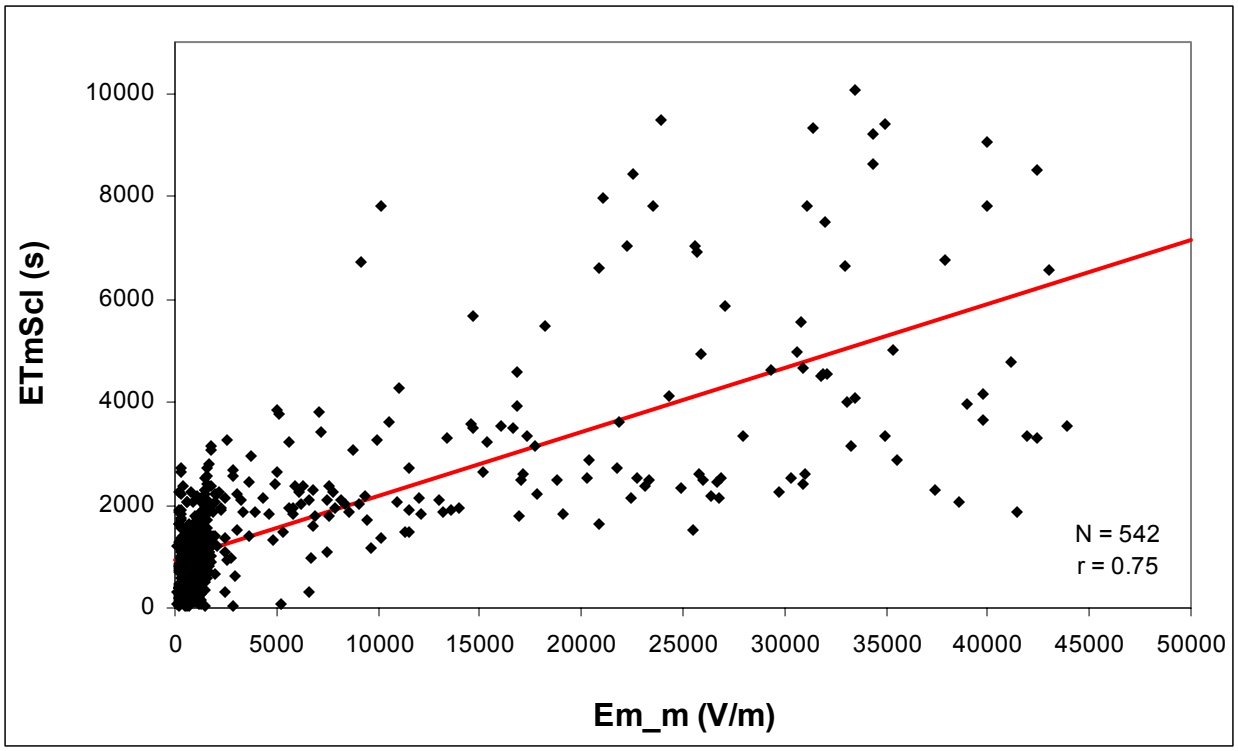

Figure 24 -- Scattergram of τ_E vs. $|E|$ for the "cldltgflt" dataset with the middle-of-anvil filter applied. Otherwise similar to Figure 5.

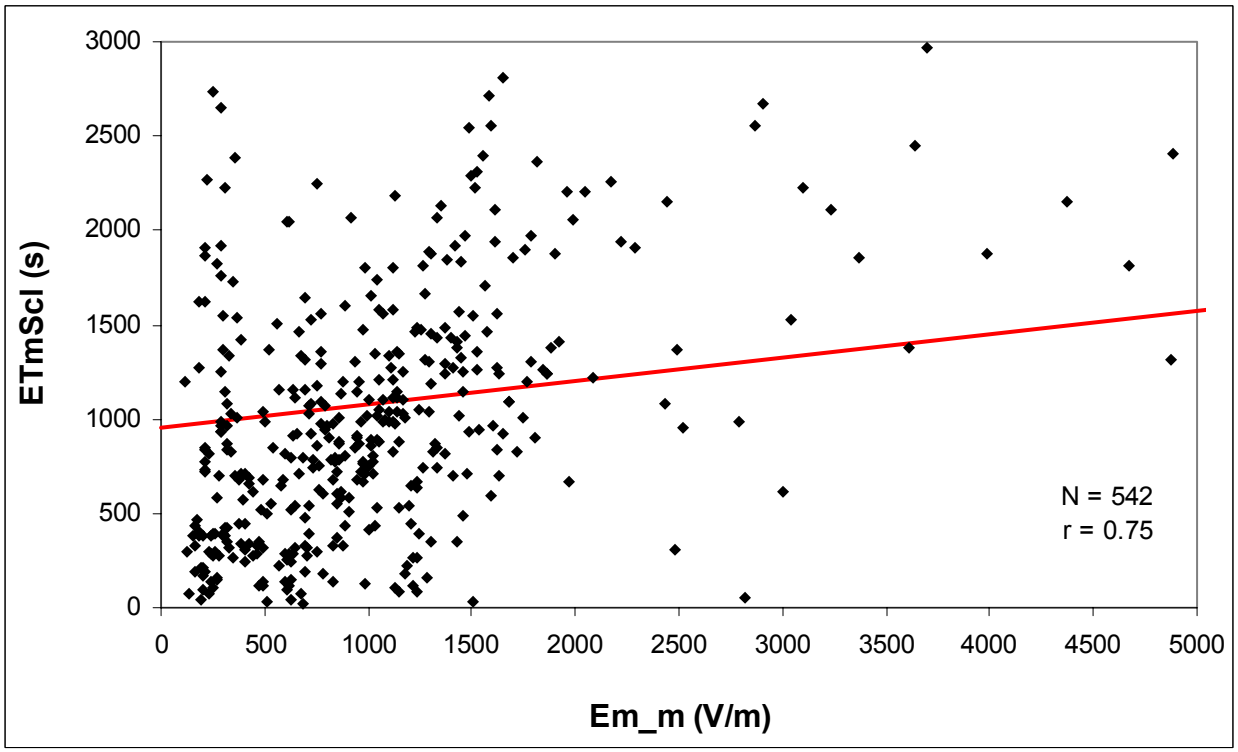

Figure 25 -- Magnification of the lower-left quadrant of Figure 24.

Case Studies of Predicted vs. Observed Field Decay

A number of case studies, recommended and initially analyzed by Jim Dye [personal communication] of NCAR, were examined in detail in an effort to validate (or invalidate) the electrical-decay model. These case studies fall into two classes. 1) There were several storms in which the aircraft apparently made multiple intersecting passes through the anvil while the electric-field intensity decreased from strong to weak (temporally, spatially, or both). In those cases it was attempted to identify the times when particular air parcels were re-visited in order to determine the decay of measured field intensity over time. 2) In several more cases the aircraft arrived late in the anvil of a storm that had been producing lightning, after the field had already decayed. In those cases it was assumed that the ambient field had been high either in the active core or at the time and location of the last lightning discharge (as indicated by LDAR sources), and the time of flight of the air parcel(s) to the aircraft location(s) was taken as an upper bound on the observed decay time. In each class, the observed decay time was then compared with that predicted by the model. This section summarizes the results of these studies.

Re-Visit Analysis

Storm days that were initially suggested for these case studies were 000613, 000614, 010604, 010615, and 010624. First the wind speed and direction over a number of passes at a constant aircraft altitude had to be estimated in order to compute the drift of air parcels with time. Examination of the aircraft winds strongly suggested that measurements from the wing sensors were unreliable, and the nose sensors were usually unavailable or untrustworthy at the altitudes of interest (apparently due to icing of the pitot tubes), so the wind was normally estimated from the propagation of the radar anvil edge. Then simple software was developed (using Visual Basic within Microsoft Excel 2000 -- software available on request) to "drift" the aircraft track progressively upwind over time and to identify all intersections of that "drifted" track with itself (using the 10-s Merged Files from the NCAR Web site). If the actual wind is uniform, constant, and equal to the estimated wind, then these intersection points correspond to re-visits of air parcels by the aircraft.

000614: An example of this procedure is presented in detail for the storm on 000614, which turned out to be our best case for re-visit analysis. Figures 26 through 28 show the

development of the anvil of interest from 2231 UT, when it is beginning to emerge at the 9 km level from a relatively new active core, until 2358, when lightning has ended and the core has all but disappeared. In Figure 26 the aircraft is still flying in an earlier anvil, Figure 27 shows one of four transverse passes across the anvil of interest, and Figure 28 shows the end of the final, upwind, longitudinal pass along the entire length of the now-dying anvil. On radar the motion of this cloud at the aircraft altitude of 9350 m appears relatively constant toward 110 deg. at 10.2 m/s. The final longitudinal pass is along the reciprocal heading of 117 deg., which appears well aligned with the wind. (Doppler data from NEXRAD, which was almost directly downwind from this anvil during its early development, suggest that the average wind speed was weaker -- somewhere between 5 and 10 m/s with a considerable gradient, both from center to edge and especially from origin to tip. Figure 29, for example, shows the NEXRAD radial velocity distribution that corresponds to the CAPPI of Figure 27. No wind-profiler data are available from KSC during the period of interest to help resolve this disagreement. Because of the flight path, however, the longitudinal pass must have intersected all of the transverse passes within a few minutes. Therefore, the exact wind speed doesn't matter much in this case, as long as its direction is correct.)

Based on the stated wind speed, Figure 30 compares the actual (red) and "drifted" (green) aircraft tracks through the anvil of 000614. The four intersections between the transverse (N-S) passes and longitudinal (SE-NW) pass are obvious on the green track, as are several other intersections that depend more strongly on the exact wind speed. This "drifted" track was used to automatically identify the intersections that are tabulated, after filtering out those for "Anvil_Type" = 0, in Figure 31.

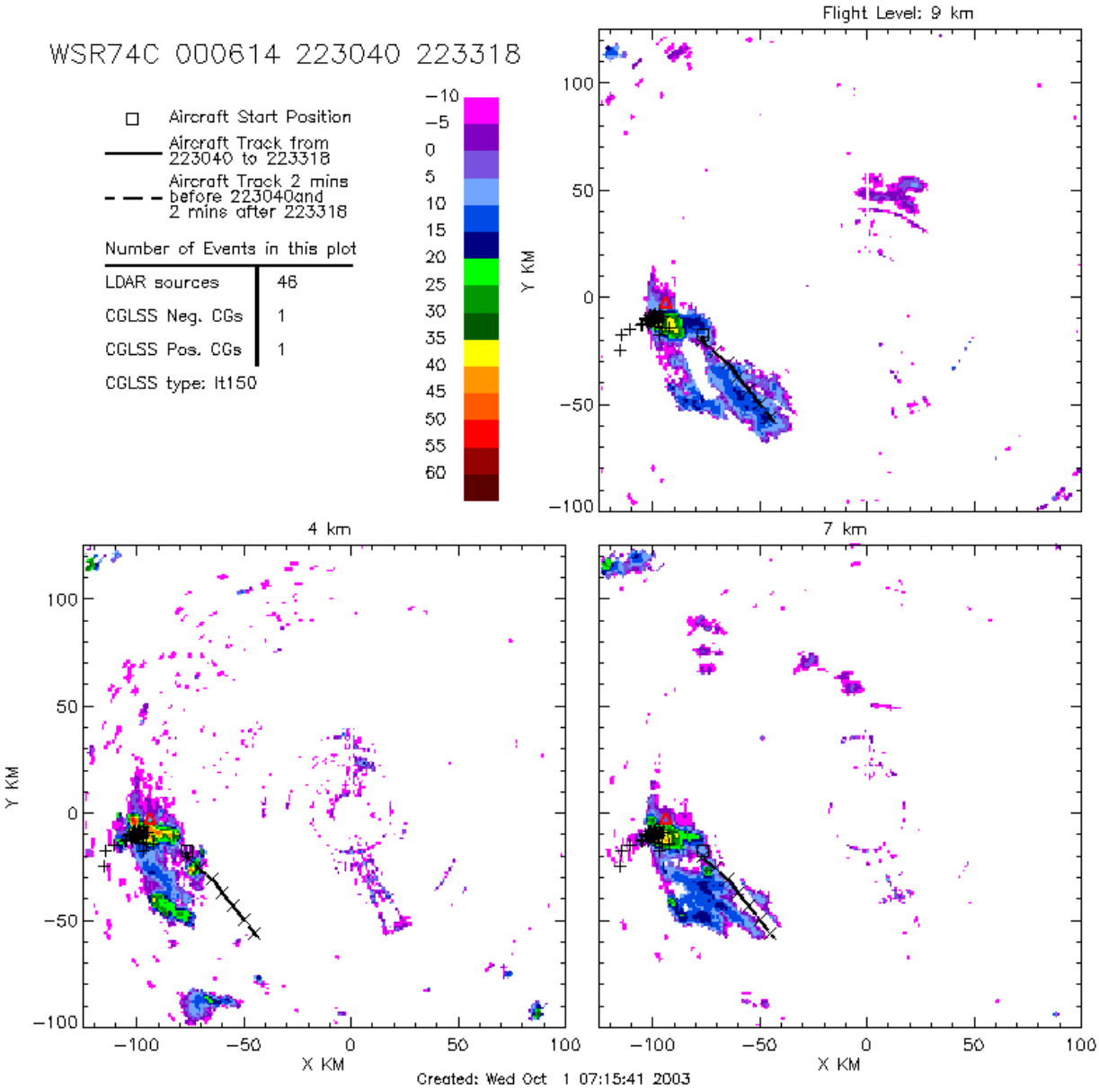

Figure 26 -- WSR-74C CAPPIs with lightning from the NCAR Web site, showing radar reflectivity at three altitudes during the onset of the anvil of interest (located at the □). The aircraft track shown is in an older anvil.

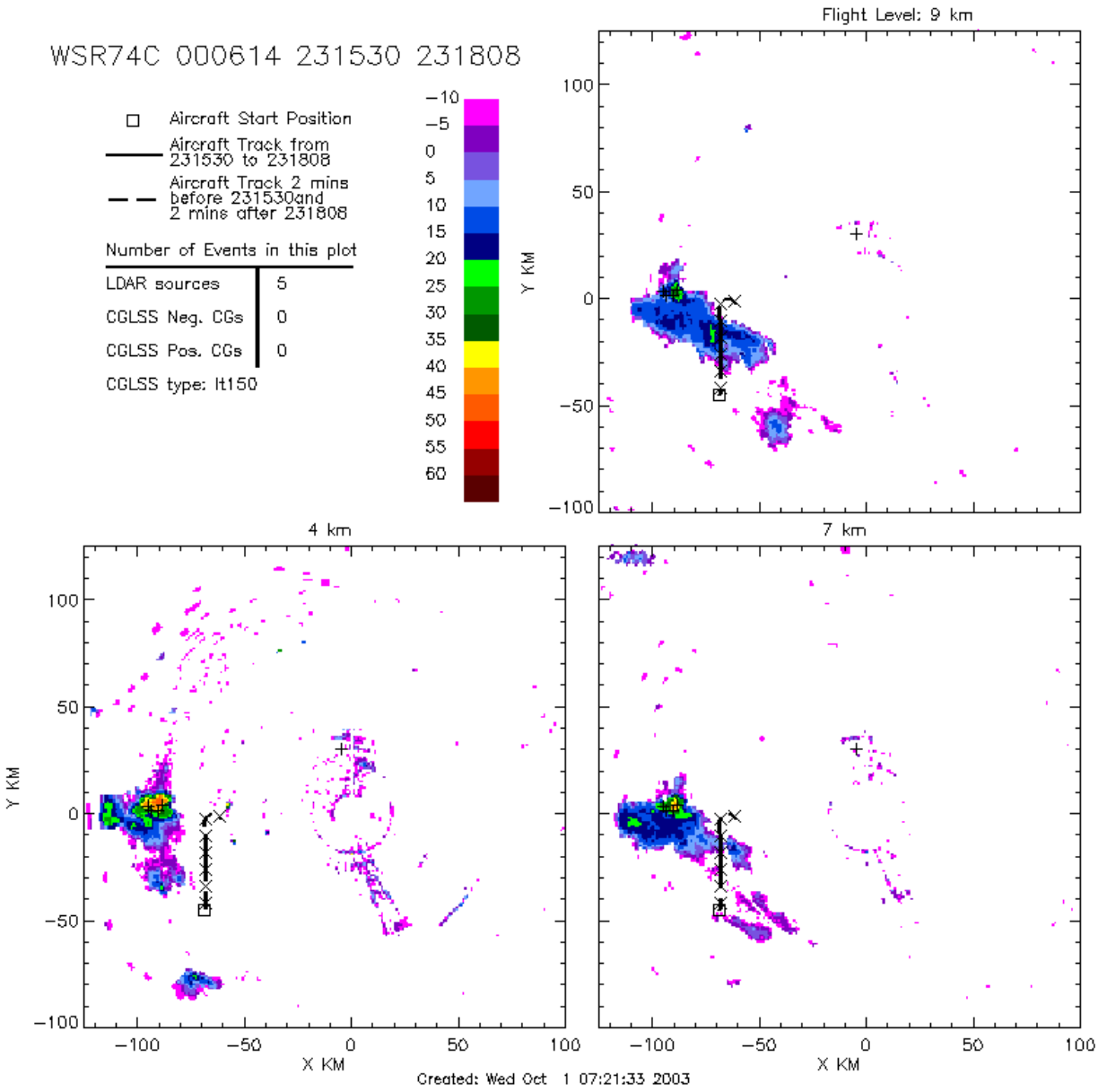

Figure 27 -- Similar to Figure 26 but 45 min. later, showing one of the transverse passes.

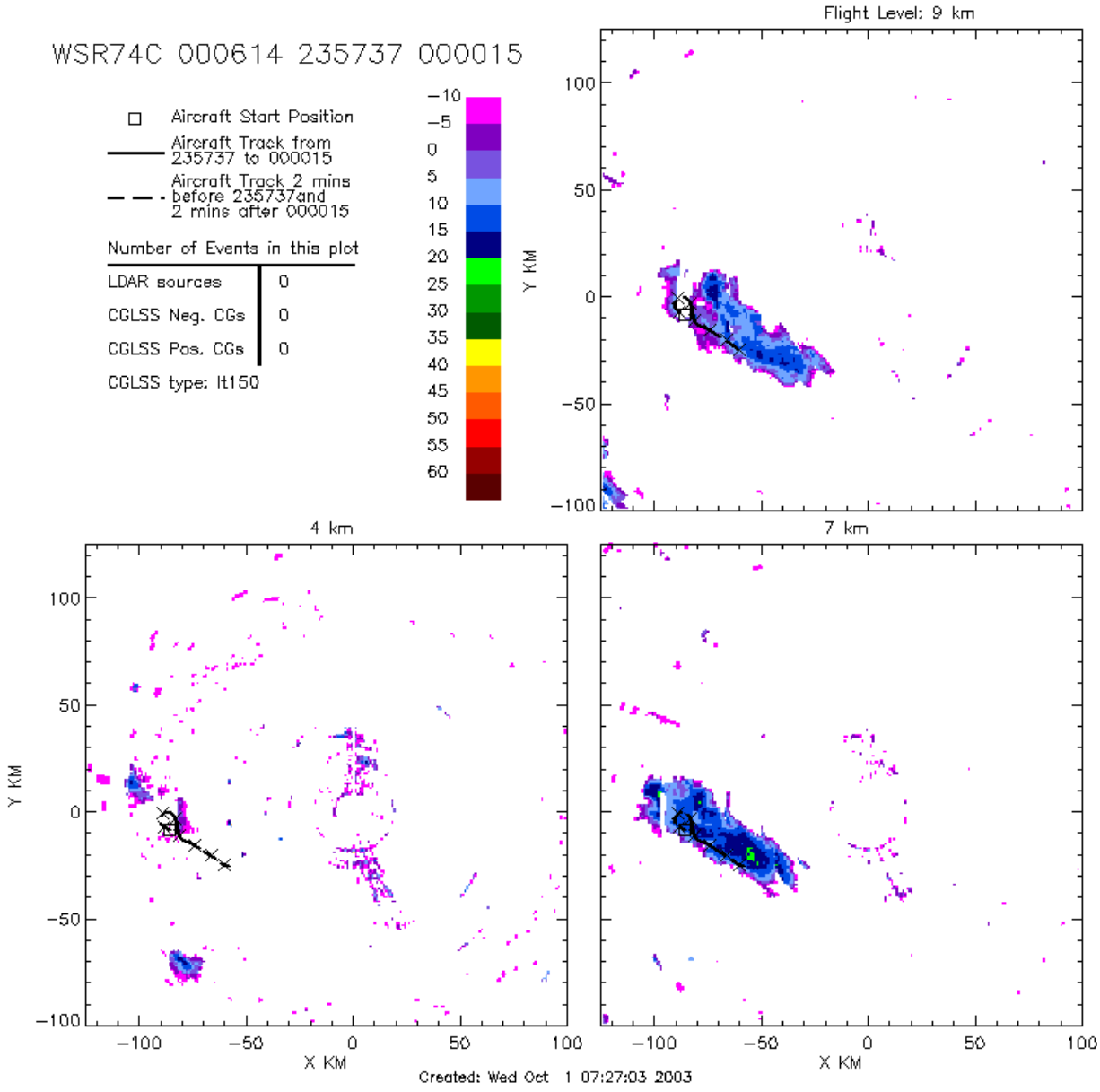

Figure 28 -- Similar to Figure 26 but 87 min. later, showing the end of the longitudinal pass.

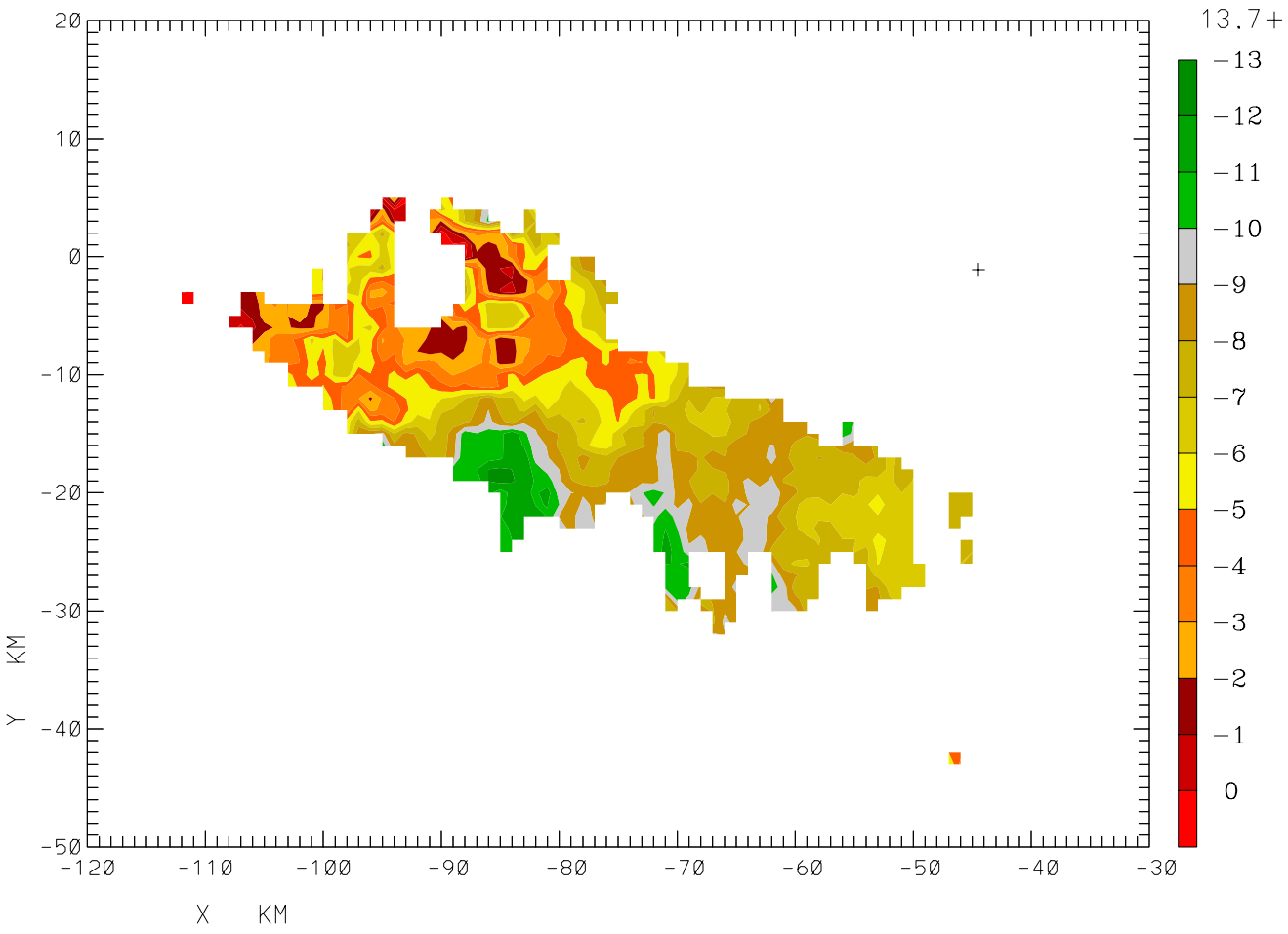

Figure 29 -- NEXRAD radial velocity field corresponding to Figure 27

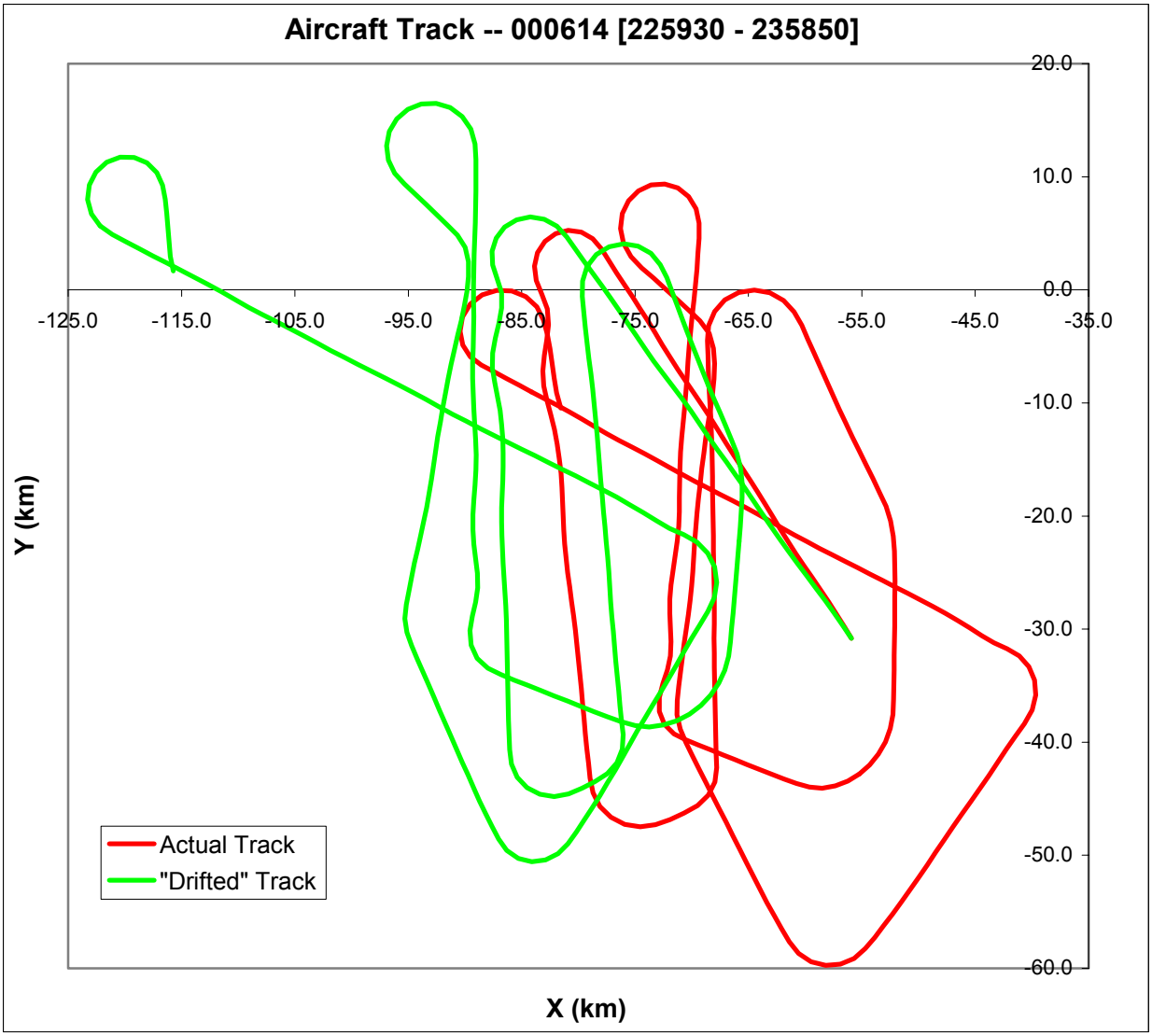

Figure 30 -- Actual (red) and "Drifted" (green) aircraft tracks during the indicated time interval on 000614, plotted on the KSC X-Y grid. Relative to the actual track only, (0,0) is the location of the Patrick AFB WSR-74C radar. The starting point is where the two tracks coincide.

Initial Time	ETmScl.	Emag	POS_Alt	Re-Visit	Re-Visit	ETmScl.	Emag	POS_Alt	Flight	Predicted1	Observed-	Predicted2	Observed-
hhmmss	(s)	(V/m)	m	Time	Sep. (km)	(s)	(V/m)	m	Time (s)	Emag (V/m)	Predicted1	Emag (V/m)	Predicted2
230130	1767	1708	9360	232240	0.49	1252	1459	9353	1270	0	1459	0	1459
231630	2047	38545	9356	235000	0.59	1221	2081	9349	2010	0	2081	0	2081
232350	438	892	9357	234820	1.66	258	568	9357	1470	0	568	0	568
233050	3155	33265	9360	235130	0.56	1006	948	9351	1240	13613	-12665	0	948
233230	2152	2445	9353	233710	0.77	2210	1960	9344	280	0	1960	0	1960
233840	1933	5790	9348	235200	0.32	1036	1097	9353	800	0	1097	0	1097
235510	816	1017	9352	235850	0.64	963	1012	9160	220	0	1012	0	1012

Figure 31 -- Table of in-anvil re-visits during flight 000614. The time of the initial visit of the aircraft to each air parcel (each row) is given in the first column, followed by three parameters corresponding to that time. The initial times that correspond to the four intersections of primary interest are shaded yellow. The time of the subsequent visit to that same parcel (based on the assumed wind) is given in the fifth column, followed by the horizontal separation (which must be less than a 2 km threshold for identifying intersections) and the corresponding values of the same three parameters. "Flight Time" in the 10th column is the interval between the two visits. "Predicted1 Emag" is the field that the model would predict at the re-visit time, given the measured field and the computed τ_E (ETmScl) at the initial time. "Predicted2 Emag" is similarly computed using the re-visit τ_E. Finally, the difference between the observed and predicted field magnitudes is indicated in the cyan-shaded columns. These values must be small or negative (as they are here) if the model is valid.

It must be recognized that τ_E, which is computed from the local cloud-physical measurements, does not normally remain constant during the time interval between visits to a parcel of anvil air. For various reasons, probably including particle aggregation, sedimentation, and evaporation, τ_E is usually smaller at the re-visit time than at the initial time, as seen in Figure 31. Therefore, we computed the model-predicted field decay using both of these extreme values of τ_E. The actual decay is expected to lie somewhere between the two predictions. In practice the observed decay is often faster than either of these predictions, however, perhaps as a result of processes not considered in the model, such as non-uniformity of cloud properties and/or turbulent mixing. Although it is not possible to prove the model's validity under these circumstances, we can develop confidence in it to the extent that the observed decay is never *slower* than that predicted from the initial value of τ_E.

In Figure 31 the longitudinal pass (2347 - 2356) is seen to have intersected parcels that had been measured during the four transverse passes at (1) 231630, (2) 232350, (3) 233050, and (4) 233840. The observed field decay is consistent with the model predictions in each case. We can loosen up this analysis as follows, however, to allow for uncertainty in the wind speed. In all cases except perhaps (2), these intersection points were very near the center of the anvil, based on time series of τ_E, R_3, and $|\mathbf{E}|$ during the respective transverse passes. Since the field magnitude on the longitudinal leg did not exceed about 2.1 kV/m (30 s average), we can assume that the anvil charge had fully decayed by the time of this pass. Since this leg was essentially parallel to the anvil development, we can also assume that the intersection points on the earlier transverse legs are correct, even if we cannot exactly predict the corresponding intersection points on the longitudinal leg because of uncertainties in the wind speed. Thus, it seems reasonable to take the maximum τ_E and $|\mathbf{E}|$ (not necessarily at the same point) from each transverse pass and extrapolate the model field decay to the time of the corresponding re-visit. This approach yields the following table, where "Decay Time" is the predicted time for the field to decay from its initial value to zero (according to the model), and "Flight Time" is the interval between first and second visits to the parcel (according to the formal re-visit analysis of Figure 31):

Pass #	τ_E (s)	$\lvert\boldsymbol{E}\rvert$ (kV/m)	Decay Time (s)	Flight Time (s)
1	2594	38.5	1997	2010
3	3155	33.3	2101	1240
4	2380	20.9	995	800

Notice that "Decay Time" is appreciably longer than "Flight Time" in two out of these three cases, which is what one would expect from the facts that we have taken maximum values of the input data and that the cloud physics (hence τ_E) is actually decaying along with the field instead of remaining constant. (The maximum τ_E measured during the transverse pass was only 1350 s, and that was somewhat upwind of the calculated intersection point with all four transverse passes.)

Pass 2 is special in that the field was already low at this down-wind location in the anvil. (The maximum $|\boldsymbol{E}|$ on this pass was 1.5 kV/m, and the maximum τ_E was only 1444 s.) Using our estimated wind speed of 10.2 m/s and the geometrical distance of 18.5 km between the intersection points on passes 1 and 2, we compute a transit time of 1814 s. The above table gives a model decay time from pass 1 of 1997 s, which is again somewhat longer than the estimated transit time.

Finally, the last LDAR source in the core of this storm occurred during the WSR-74C scan that ended at 233355 [Jim Dye, personal communication]. (This analysis strictly belongs in the next sub-section, but it was decided to keep all consideration of each storm together.) Thus, at least 965 s elapsed until the peak field of 2.1 km was penetrated during the longitudinal pass, although the A/C did not make it's closest approach to the core until about 2357, at least 1385 s after the last LDAR source. Neither interval is inconsistent with the maximum τ_E of 1350 s that was measured on this longitudinal pass, nor with the larger maximum of 1701 s that was recorded at 235900 - 235930, near the end of the turn and during the descent to 8.0 km for the last leg of the flight.

In conclusion, the 000614 storm appears consistent with the model.

010615: The only other reasonably satisfactory case for re-visit analysis turned out to be the storm on 010615, shown on radar in Figure 32. The winds in this storm are the big uncertainty. Previously I had used a wind of 7 m/s toward 135 deg. [Willett, ABFM Workshop of May, 2003], which approximates the direction of drift of the radar anvil edge (and the convective line and the aircraft track) from NEXRAD. (The more severe scan gaps on the WSR-74C make wind estimation almost impossible.) Unfortunately, the propagation of a line does not necessarily give the motion of the individual parcels in that line! There are no wind-profiler data for the storm interval, but if we take the aircraft nose winds (only available for the 8.0 km passes) seriously, we get an average wind at that height (after filtering out intervals with significant pitch and roll) of 9.6 m/s toward 077 deg. (The wing winds, similarly filtered,

average 10.7 m/s toward 074 at 8.0 km and 10.4 toward 123 at 8.6 km, although their direction varies wildly from pass to pass.) Based on the extreme uncertainty of the wing winds, the lack of profiler data, and the fact that even the convective cores at 4 km seem to be moving more toward the E than the SE, there is little evidence of strong wind shear over the 600 m between flight levels in this storm.

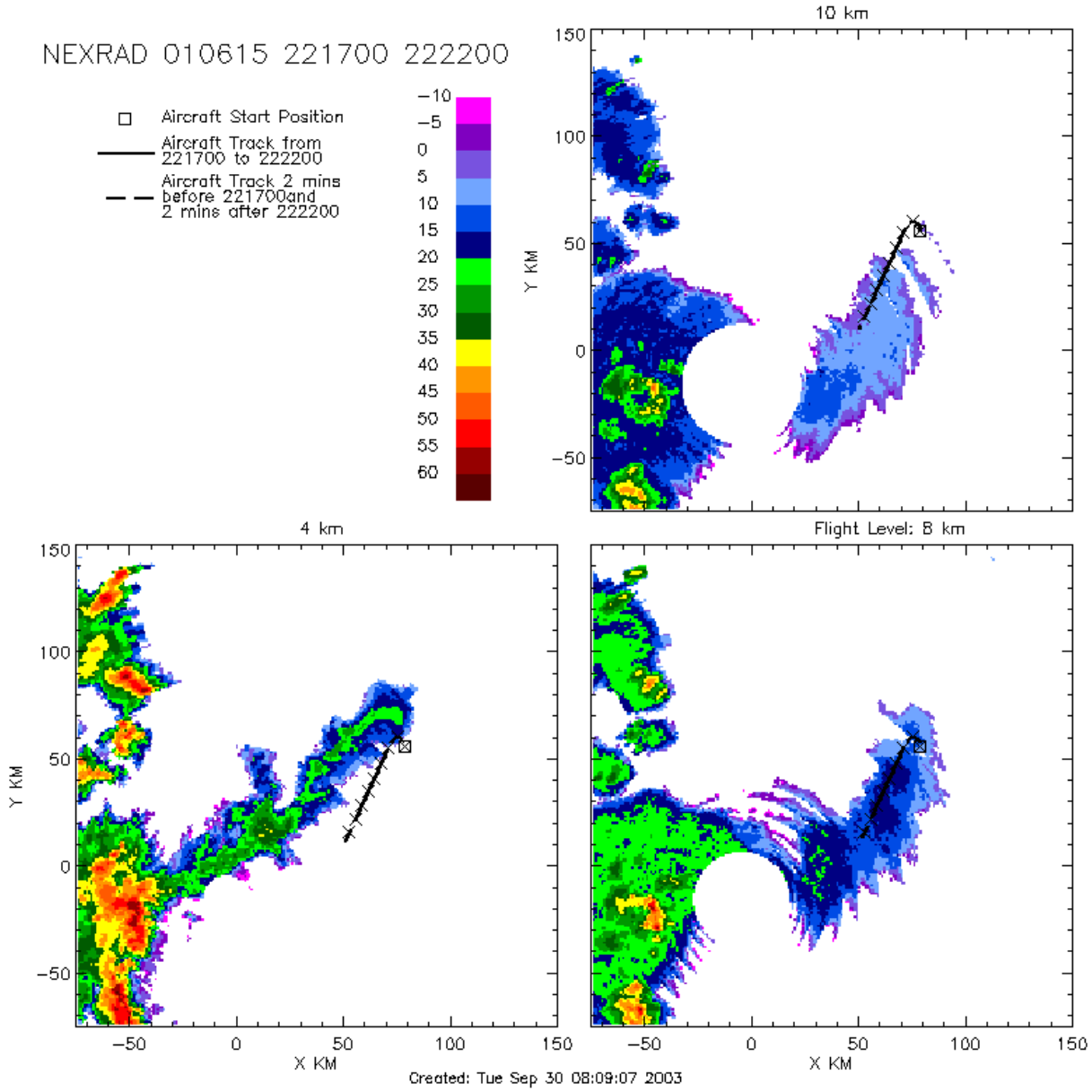

Figure 32 -- Like Figure 26 but without lightning and from NEXRAD data during pass 3 in the anvil of 010615.

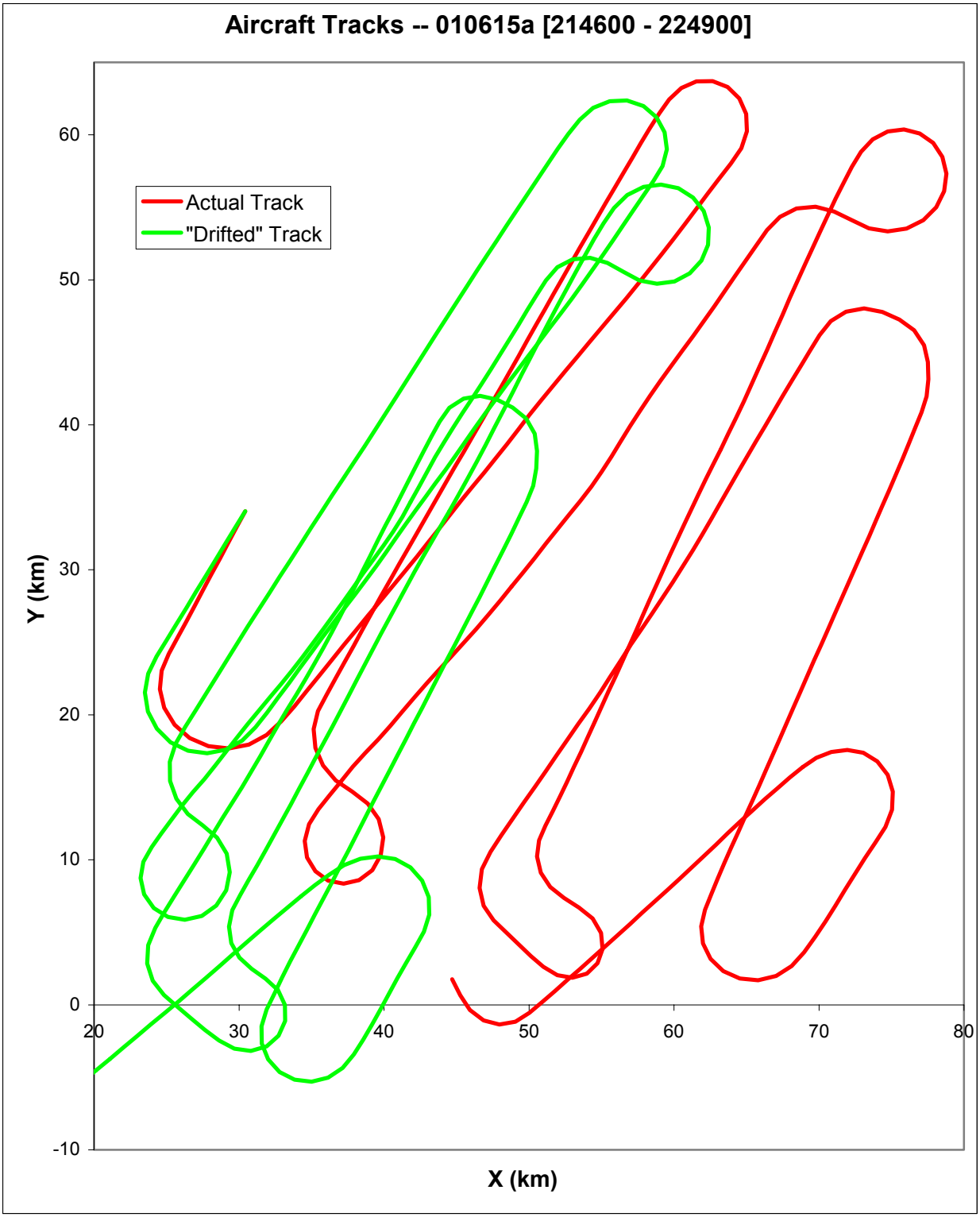

Figure 33 -- As in Figure 30 for the storm on 010615.

Using the above wind estimate at both levels, we have computed the "drifted" track shown in Figure 33. The basic

result of re-visit analysis on this track is that there were four parallel passes (transverse to the anvil propagation) that were essentially coincident: (1) 214910-215310, (2) 220800-221210, (3) 221810-221920, and (4) 222910-223320 -- (3) being in the opposite direction from, and only coincident with part of, the other three. Passes 1 and 2 were at 8.6 km altitude, whereas (3) and (4) were at 8.0 km.

Comparing passes 1 and 2, we find that the observed field did not decay as fast as predicted over the nearly constant interval of 1130 - 1140 s between passes (they are in the same direction) except toward the NE end (although the actual field magnitude does decrease everywhere except at the extreme SW end). This apparent model violation might be because the estimated wind is incorrect and/or because there continues to be development in the anvil at this stage of the storm. (Either of these excuses is supported by the observation that τ_E increases from pass 1 to pass 2 throughout their middle sections.)

Comparing (2) and (3 -- at lower altitude) the model appears reasonably valid over the interval of 510 - 360 s (depending on position along the passes because they are in opposite directions), although the initial fields on this part of pass 2 are not very high. Comparing (2) and (4 -- also at lower altitude) provides more convincing agreement over the interval of 1270 s, since the initial fields over at least the first part of this coincidence are moderately large -- up to 16.9 kV/m. Finally, comparing (3) and (4 -- same altitude but without much overlap) over the interval of 760 - 910 s is uninspiring: Although the fields do decrease throughout, they are pretty small initially.

The big question throughout the above discussion is whether the estimated winds are correct. If we continue to assume that these four passes overlap (in other words, that the southeastward drift of the line determines the wind component normal to the line) but we take the maximum τ_E and the maximum $|\boldsymbol{E}|$ -- 30 s averages, not necessarily at the same point -- from each pass (effectively assuming that the component of the wind parallel to the line is unknown), we get the table below:

Pass #	τ_E (s)	$\lvert\boldsymbol{E}\rvert$ (kV/m)	Decay Time (s)	Flight Time (s)
1	4662	38.6	3597	2400
2	2722	16.9	920	1270
3	3052	1.8	109	>760
4	1743	1.1	40	--

"Flight time" in this table is the interval from the pass in question until pass 4 (the first time when we can be sure that

|***E***| is small throughout, since the overlap with pass 3 is fairly short). In this treatment the model appears valid between (1) and (4), in that the flight time is shorter than the model decay time, but it might or might not be violated between (2) and (4). Note, however, that the assumptions made here are not entirely consistent: We are effectively assuming that the wind component normal to the line (9.6 m/s projected from 77 deg. onto 135 deg.) is only 5.1 m/s, not the radar-estimated value of 7 m/s. Further, we have only considered the segments of the passes that coincide according to the "drifted" track in Figure 33. Both of these objections can be addressed by reverting to the May 2003 analysis, where the pass durations change somewhat to (1) 214830-215530, (2) 220620-221240, (3) 221720-221910, and (4) 222700-223230. The above table then becomes

Pass #	τ_E (s)	|***E***| (kV/m)	Decay Time (s)	Flight Time (s)
1	5676	38.6	4379	2250
2	2729	17.9	978	1190
3	3052	1.8	109	--
4	3130	1.8	111	--

but the conclusions are the same. In this second version of the table (3) coincides only with (1), not with (2) nor (4). The time interval for this coincidence ranges from 1520 to 1310 s. Although the maximum decay time on the relevant (latter) part of (1) is only 1298 s, this is not much smaller than the observed range of flight times (nor is the model violated point-by-point).

Finally, the last LDAR flash along this line of storms occurred during the WSR-74C scan that ended at 212534 [Jim Dye, personal communication]. The first pass with only low fields was (4) -- pass 3 had |***E***| as high as 7.2 kV/m on its SW extension beyond the coincidences listed above. The maximum |***E***| on pass 4 of 1.7 kV/m was measured near the SW end, coincident with the largest τ_E of 3130 s, during the 30 s interval beginning at 222830. Thus, the elapsed time from last lightning to low-field measurement was at least 3776 s, which compares favorably with either maximum τ_E (4662 or 5676 s) that was measured at the SW end of pass 1.

In conclusion, 010615 is not a particularly good case, but it does not appear to invalidate the model.

000613: Although the storm on 000613 appears to be the ideal anvil case in many ways, it is flawed by three main problems: 1) The aircraft is consistently flying above the main radar reflectivity and is near the upper edge of the anvil for most of the time (see Figures 34 and 35).

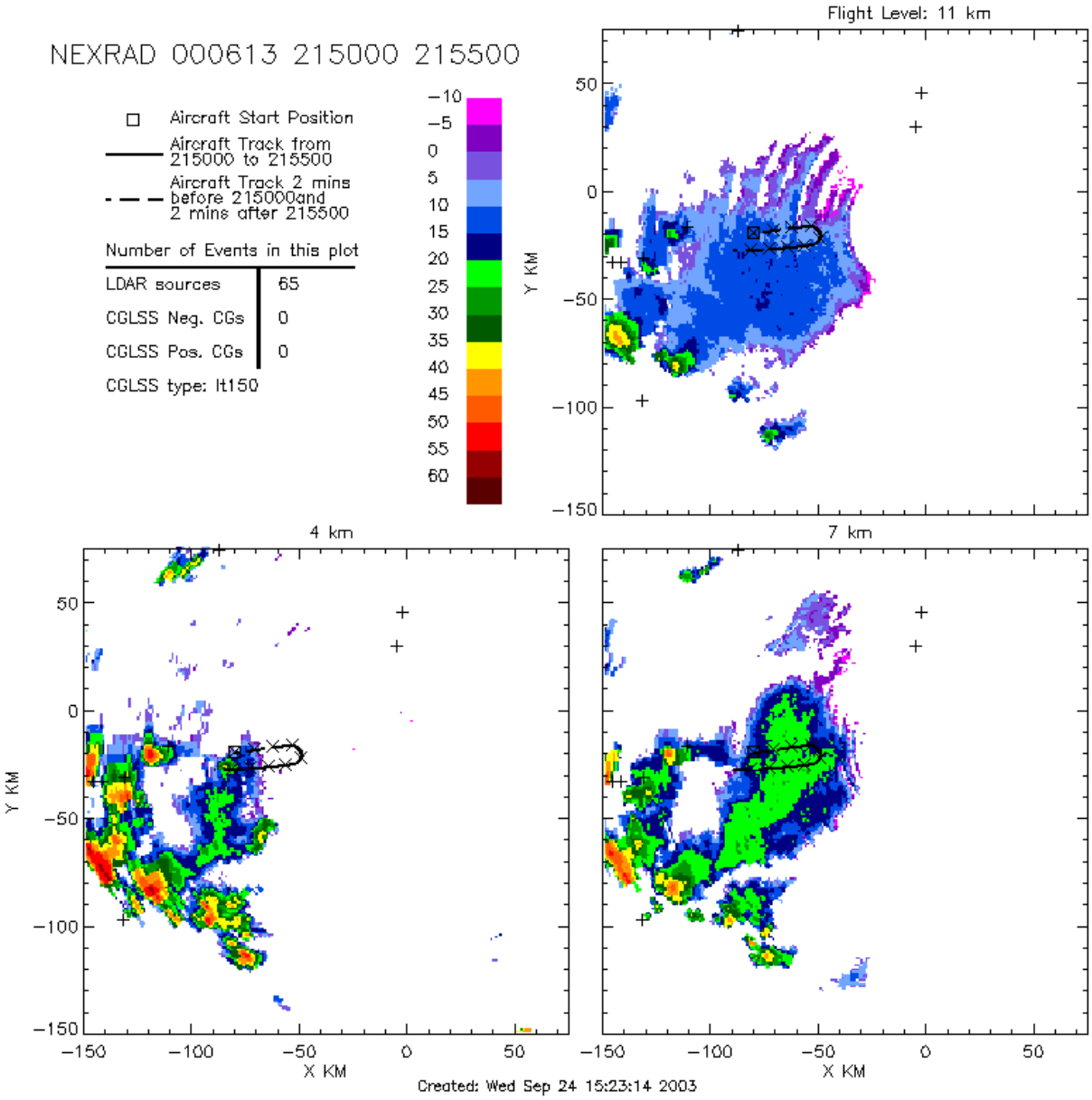

Figure 34 -- Like Figure 26 but from NEXRAD data during the 11.2 km passes with highest field in the anvil of 000613.

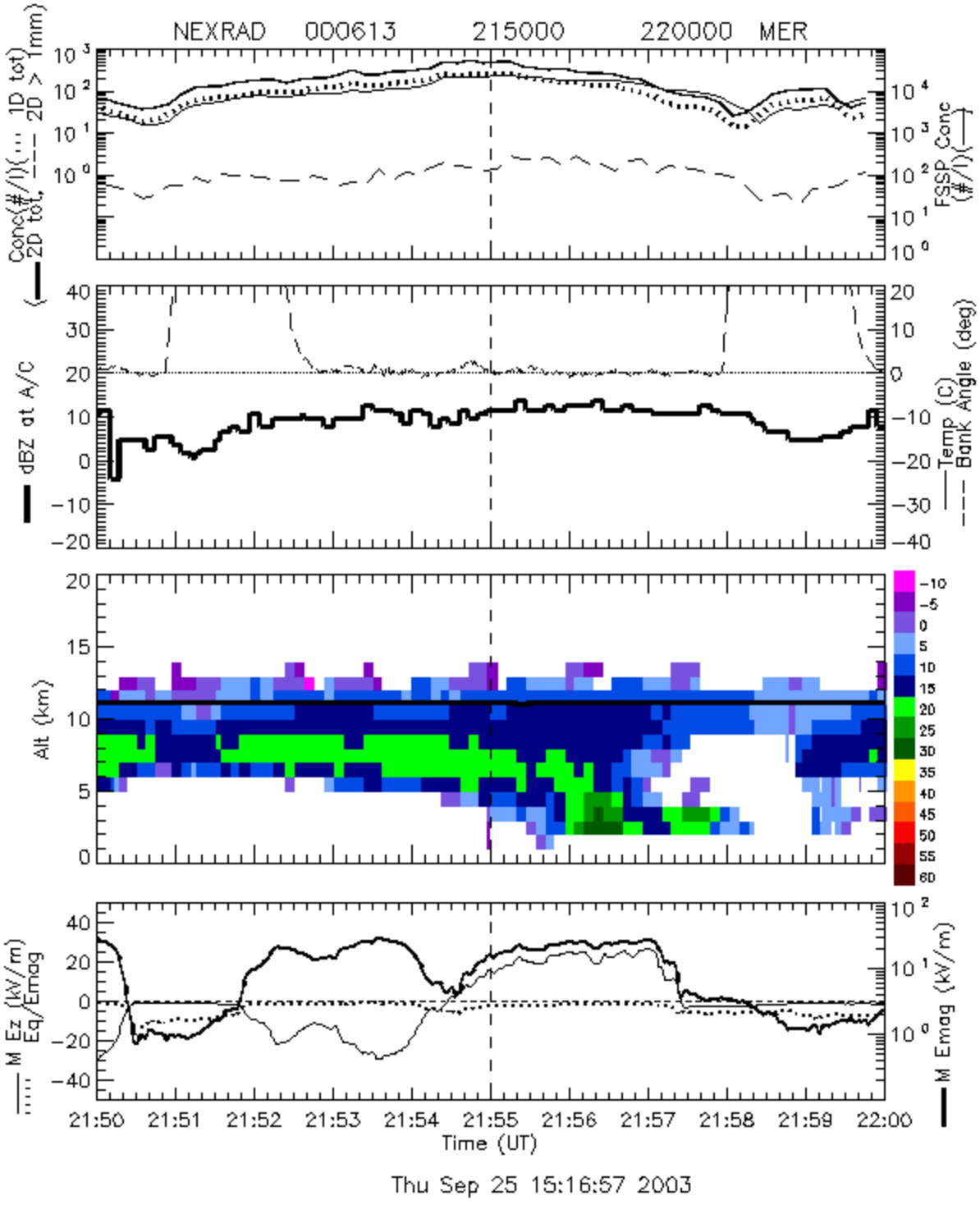

Figure 35 -- "MER" plot corresponding to Figure 34 -- a time-series plot showing the radar-reflectivity "curtain" and on-board measurements along the aircraft track. For a more detailed explanation, see the NCAR/ABFM Web site.

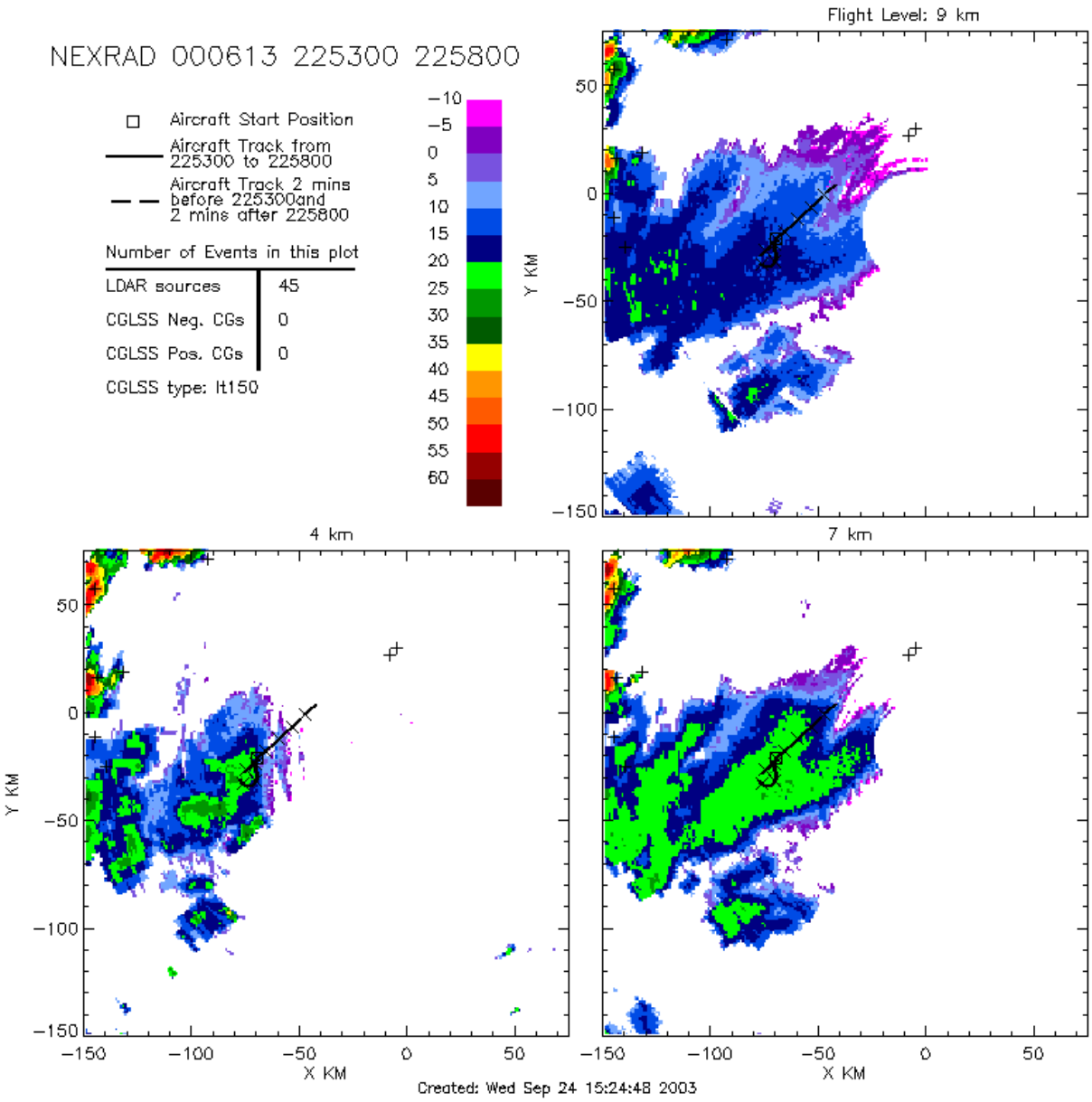

Figure 36 -- Like Figure 26 but from NEXRAD data during the two, elevated-field passes in the quiescent phase of the anvil of 000613.

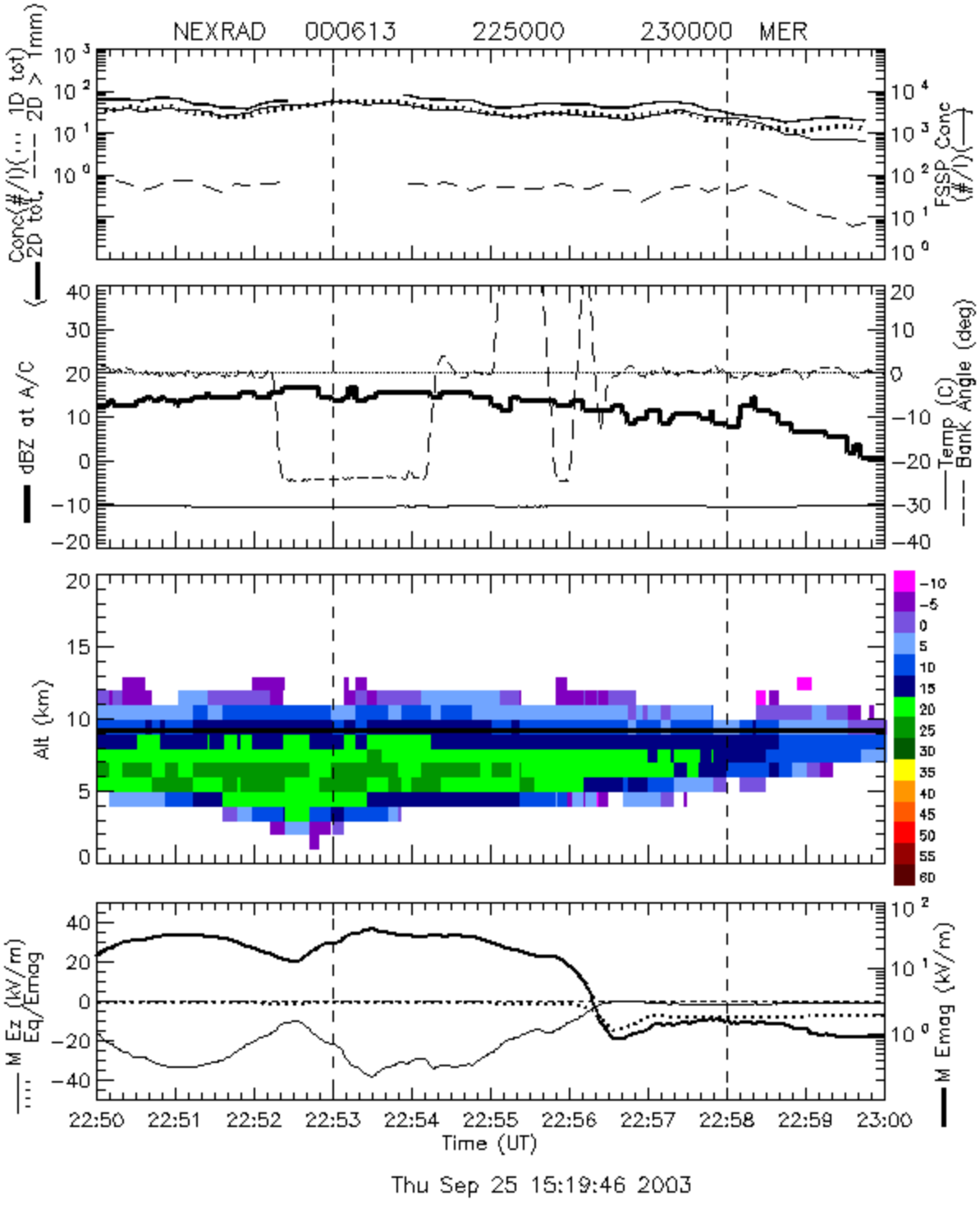

Figure 37 -- "MER" plot as in Figure 35, but corresponding to Figure 36.

2) There is evidence [Jim Dye, personal communication] of continued convection during the early period. This appears mainly confined to a small core toward the W end of the E-W tracks (see Figure 35). 3) In the later, quiescent part of the anvil evolution (2249 - 2256), when the aircraft made passes first at 9.3 km and then at 8.0 km, the only elevated fields appear to be over melting precipitation (see Figures 36 and 37). Since these fields could be due to some precipitation mechanism, they don't have to obey the computed decay times.

In spite of these problems, we can still compare decay times, as long as we realize that the computed decay times are significant under-estimates because of (1) above. For the 11.2 km passes (2113 - 2231), even though we aren't very confident of our wind estimate from the motion of radar cloud boundaries (9.2 m/s toward 040 deg.), we know that the E-W passes are roughly cross wind, whereas the last SW-NE pass is roughly parallel to the wind. Since the fields throughout this last pass (222540 - 223430) are low [Jim Dye, personal communication], we don't really care what part of this pass intersected the E-W passes; and since the latter are roughly cross-wind, we know reasonably well where on those E-W passes these intersections occurred. Fortunately, these intersections are all toward the middle or E end of these legs, so we shouldn't have to worry about that pesky convective cell mentioned in (2) above. My previous re-visit analysis [Willett, ABFM Workshop, May 2003] showed only two intersections with significant initial fields: 16.7 kV/m at 215020 and 8.8 kV/m at 215410. (In Figures 35 and 36 note the strong gradient of $|\boldsymbol{E}|$ along these transverse passes, which still might have to do with that convection at their western ends and which makes the exact intersection points fairly critical.) The apparent re-visits to these parcels on the SW-NE pass occurred roughly 2000 s later and found fields less than 1 kV/m in each case. In the former case the initial (larger) τ_E was only 651 s, and in the latter it was 3387 s; in neither case is the model violated.

There were NE-SW passes through this anvil at lower levels (two pairs at 9.2 km and one pair at 8.0 km) along essentially the same geometrical track [Jim Dye, personal communication]. To the extent that this track is still parallel to the wind, we are in good shape for computing intersections. Even if winds aren't exactly parallel to the track, we can assume approximate cross-track uniformity, based on the quiescent structure of this system [Jim Dye, personal communication]. Unfortunately, the scan gaps on the radar data make it impossible to estimate the winds at these levels, the nose wind system was only working for the latter half of the 8.0 km leg, and there are no relevant data from the KSC wind profiler. Further, the elevated fields,

found only on the first pair of passes at 9.3 km, appear to me to be due to melting precipitation, as mentioned in (3) above. (It is suggestive that there's a minimum field on both of these pass pairs right over the thickest part of the "anvil" -- see Figure 37 for one example.) Finally, the field on the last pass pair at 8.0 km seems to be higher than that on the preceding pass pair at 9.3 km, suggesting again that we are skimming the top of the electrified region or that there is a weak generator operating.

Overall Conclusion: This probably isn't a good day for model testing.

010604: The other two storm days that are listed at the beginning of this section (010604 and 010624) are both now judged unsuitable for re-visit analysis, based on evidence of continued development (and corresponding electrification) in the anvils [Jim Dye, personal communication]. Typically this "secondary development," as it will be called here, is manifested by a thickening of the anvil and an increase of the radar reflectivity in its middle and lower levels that are relatively uniform over a fairly large horizontal area (in contrast to the convective development that is characteristic of thunderstorm cores). As such, it is reminiscent of the development of stratiform precipitation, although rain often does not reach the ground in these cases. The ABFM data strongly suggests that this secondary development is associated with charge separation, but this is properly the subject of a separate study. In any case, 010604 appears to be dominated by secondary development in what started out as an ordinary anvil. I had thought before the May 2000 workshop that the increases in $|\boldsymbol{E}|$, τ_E, and/or R_3 between apparent visits to the same parcel were mostly due to incorrect wind estimates. Now I don't think this can be true because the wind estimate (17.7 m/s toward 104 deg. from the NEXRAD CAPPIs) seems fairly solid and because, in this broad and relatively uniform (at least in terms of reflectivity) cloud, small wind errors shouldn't have sent us that far astray. Drifting the track with any reasonable wind indicates that the only parcel re-visits occur soon after the A/C changes from N-S (transverse) to ESE-WNW (longitudinal) passes at about 2108. By the time these longitudinal passes begin, there is already reflectivity showing up at the 4 km level pretty much everywhere beneath the A/C. Another problem is that the re-visits that I found were mostly between the early transverse passes at 9.3 km altitude and the early longitudinal passes at 9.9 km. (The later transverse passes at 9.9 km apparently were too far out in the early anvil to coincide with any of the longitudinal passes.

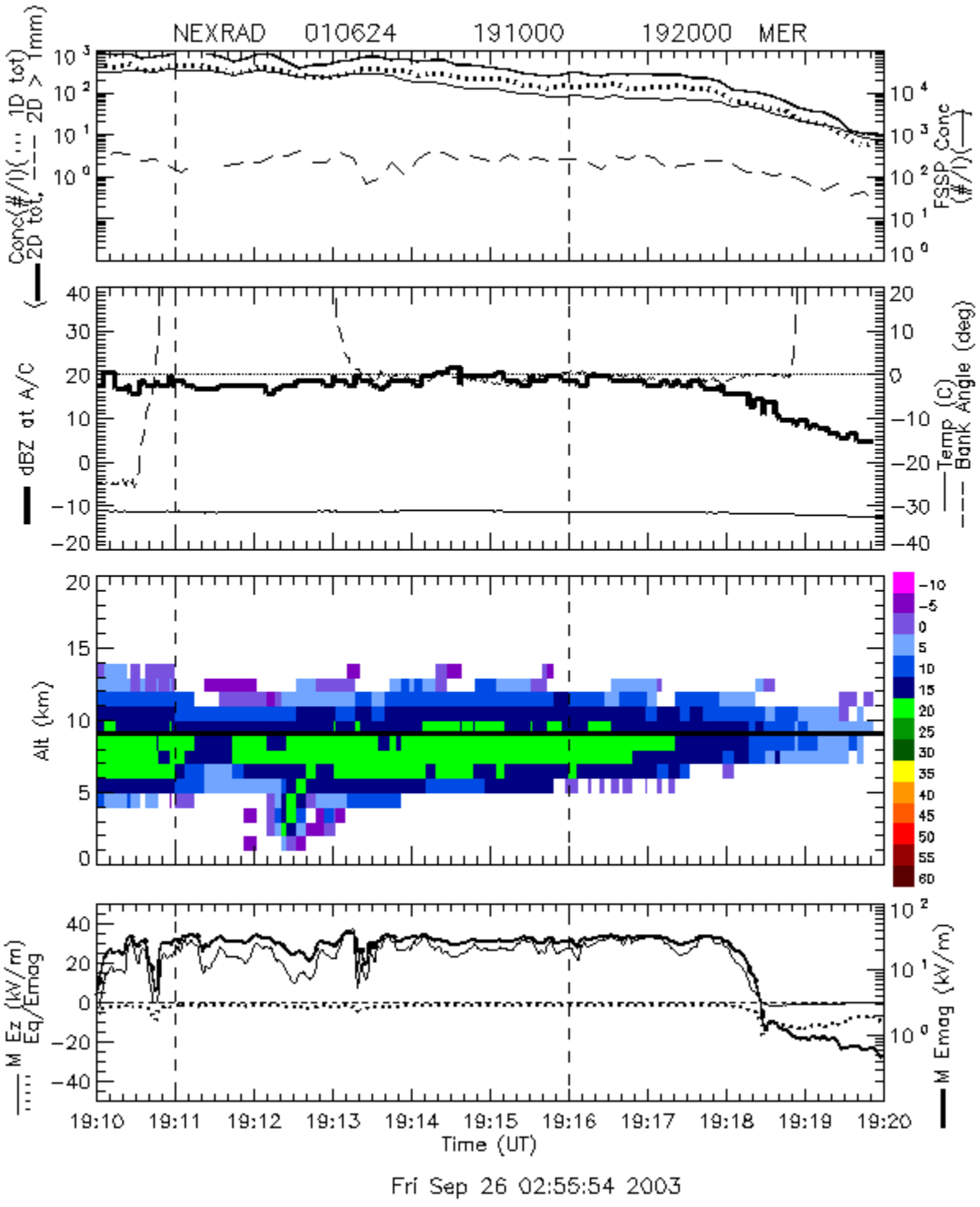

Figure 38 -- "MER" plot as in Figure 35, but for storm 010624.

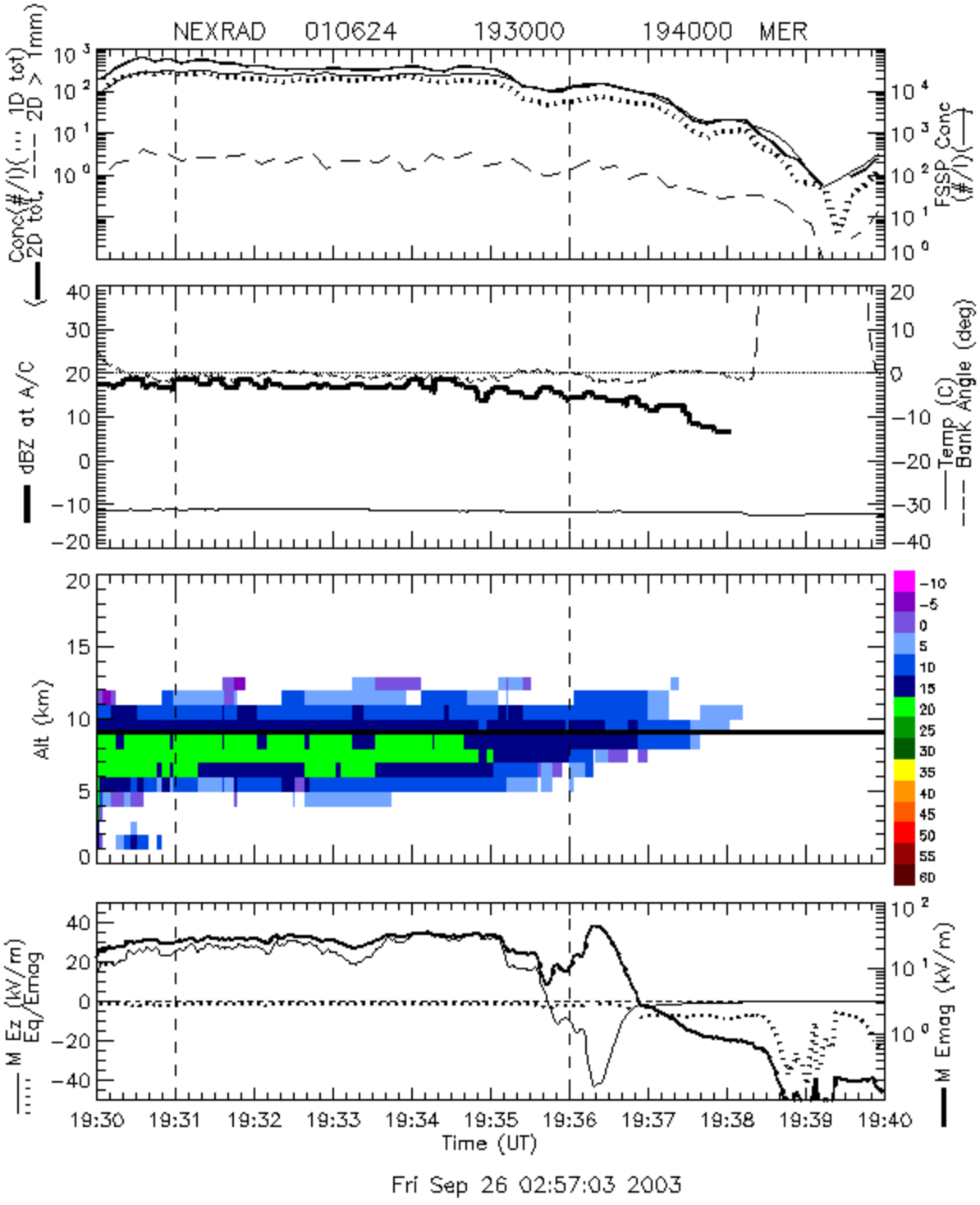

Figure 39 -- "MER" plot as in Figure 35, but for storm 010624.

Similarly, the later transverse passes at 9.3 km were probably too far in in the late "anvil" to coincide with any of the transverse passes, although I didn't actually examine these late passes because of the conclusion, even then, that this was no longer an anvil.)

010624: The situation with the massive, tornadic storm system of 010624 is similar, though more subtle. My previous re-visit analysis of this storm [Willett, ABFM Workshop, May 2003] had indicated numerous cases of increasing $|\boldsymbol{E}|$, τ_E, and/or R_3 between apparent visits to the same parcel. I had thought these problems due primarily to a faulty wind estimate derived from the NEXRAD CAPPIs (15.3 m/s toward 038 deg.). A perusal of the NEXRAD Doppler data for this storm [Monte Bateman, personal communication] did indeed indicate that, although I had gotten the wind direction right, I had significantly underestimated the wind speed for this day. It's not easy to pick a single speed from the NEXRAD Doppler plots, but I now estimate roughly 19 m/s, in good agreement with Jim Dye [personal communication]. Unfortunately, the new re-visit analysis is still loaded with anomalies. Even if I filter out cases with core_20km = 1, LDARpm5 > 2, and CGpm5 >= 1 (only 19, 10 s revisit times remaining, almost exclusively from the latter half of the long parallel passes, 191350 - 191920 and 193300 - 193820), I still get cases where the observed field, although decaying somewhat, is not consistent with the model (notably 191700 - 191710 vs. 193610 - 193620, associated with the apparently inexplicable field reversal to a maximum near the end of the second of these passes -- compare Figures 38 and 39). Jim Dye's [personal communication] assessment is that this case is another example of the "secondary development" that was described under case 010604 above. From about 1820 to 1930 a region of higher reflectivity gradually expanded at the 7 km level. The aircraft was flying above the SE extension of this region, where the storm no longer had the appearance of a line of strong convection. Therefore, this is probably not a simple case of anvil decay.

Time-of-Flight Analysis

Storm days that were initially suggested for these case studies were 000611, 000614 (an earlier storm on this day), 000628 flight 1, 000628 flight 2, 010527, 010605, and 010625. (In addition, we have already discussed this type of analysis of the storms on 000614 at 2357 and on 010615 at 2228.) Of these, the anvil of 000611 was only penetrated on the edge at about 183830, the clouds of 000628-1 (1414 - 1422) and of 010605 (1825 - 1845) are now agreed not to be anvils, and I am unable to

decipher the development of the storm of 000628-2 (1830 - 1834), which developed directly over the radar. The most interesting of the remaining cases is 010527.

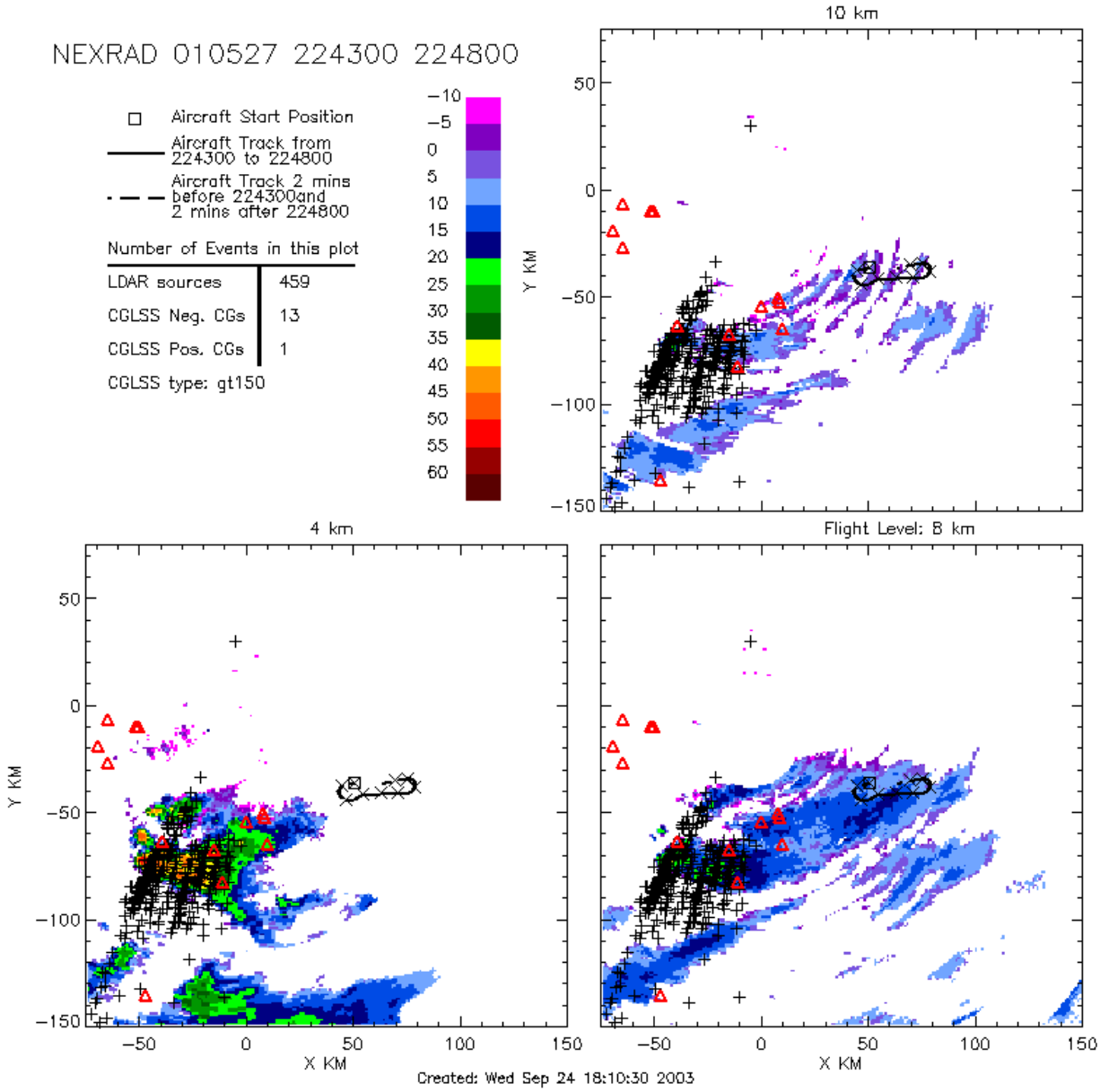

Figure 40 -- Like Figure 26 but from NEXRAD data during the highest-field pass in the anvil of 010527.

010527: This is the clearest example of this type of analysis. Between 2158 and 2322 the aircraft flew several passes at 8 km altitude through this relatively thin anvil before entering a region of apparent stratiform precipitation (and much higher fields) that had developed downwind of the

active core. During these anvil passes the highest field, $|\boldsymbol{E}| \approx$ 3 kV/m, was encountered at 224430 in a radar return of about 15 dBZ where the anvil was 4 km thick (see Figure 40). The maximum electrical decay time in the anvil, τ_E = 2944 s, was calculated for this same aircraft location -- KSC X-Y position, [59.0, -41.2] km. The anvil-feature velocity at 8 km altitude has been estimated from the NEXRAD CAPPIs to be about 18 m/s toward 070 deg. Thus, we can look backwards in time to find the closest upwind LDAR sources and compute the time required for the air parcels that might have been involved with them to drift to this aircraft position.

NEXRAD Frame (hhmm)	Nearest LDAR [X,Y]	Range to A/C (km)	Time Diff. (s)	Max. Drift (km)	Within Range?
2218	[22,-52]	38.5	1590	28.6	No
2213	[23,-60]	40.6	1890	34.0	No
2208	[16,-54]	44.9	2190	39.4	No
2203	[17,-61]	46.4	2490	44.8	No
2158	[13,-55]	48.0	2790	50.2	Yes

The above table lists the starting time of several consecutive NEXRAD frames and the position of the nearest LDAR source during that frame. The range from that LDAR source to the aircraft location is given in the third column, and the maximum time interval between that source and the aircraft measurement of maximum field is listed in the fourth column. The fifth column gives the drift distance over that time interval at the estimated wind speed. (This drift distance must be at least as large as the range in order for air parcels that were affected by lightning to be measured at the aircraft.) This presentation suggests that lightning-affected air must have aged at least 45 min. before being measured. Comparing this with the maximum observed τ_E of 49 min. gives reasonable agreement. The CAPPIs for the NEXRAD frame spanning 2158 - 2203 are shown in Figure 41.

000614: No field readings were obtained until 2130, and no 2D-C data was recorded until 214130, so we missed the first (best) pass through this anvil. The second and third passes gave a maximum τ_E of 659 s at 214500 - 214530, with a maximum R_3 of 10 dBZ during the previous 30 s interval. The relevant section of the anvil apparently began forming about 1944, so the flight time is on the order of 2 hr. to near-zero fields. This is not very meaningful since the measured τ_E is so short.

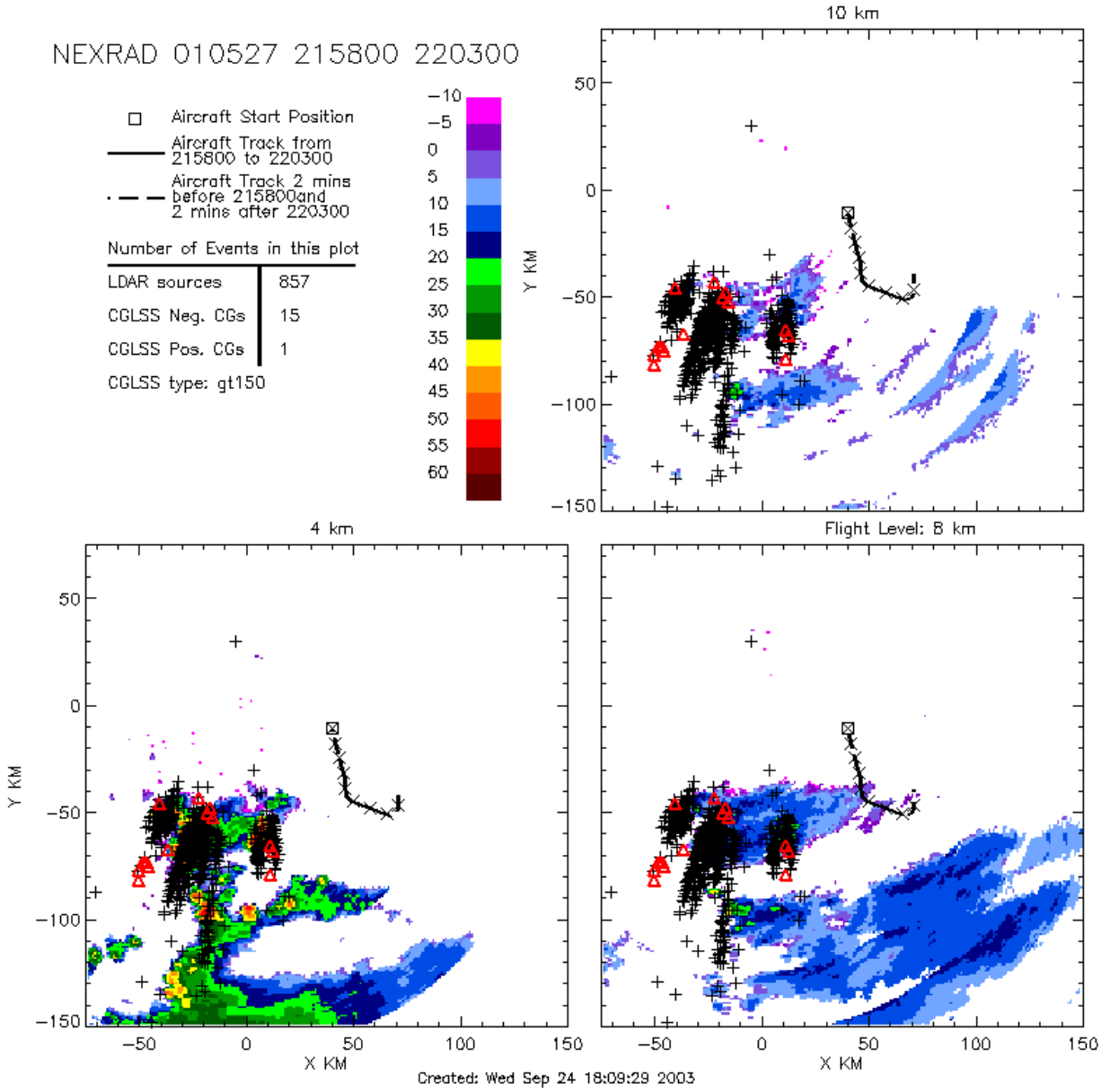

Figure 41 -- Like Figure 26 but from NEXRAD data during the latest likely exposure to lightning of the air that was measured during the pass that is shown in Figure 40.

010625: This storm began at the extreme lower-left corner of the WSR-74C CAPPI, so I'm not sure of it's lightning history, but the last CG flash appears to have occurred in the core at about 1833. Unfortunately, the only aircraft penetration of anvil that does not extend below 5 km altitude was 1953 - 2000. During this interval the field was weak and τ_E < 1000 s, although the aircraft appeared to penetrate returns of ~15 dBZ at 195920. (Later, the aircraft encountered fields of almost 3 kV/m twice,

but both were above precipitation extending well below 5 km.) Thus, this case does not give us much to work with.

Conclusions

The present study has failed to turn up any clear-cut violations of the electrical-decay model but without clearly demonstrating agreement between the model and observations. The main problem here is that an observed time for field decay to near zero can be either shorter than the predicted decay time (because of processes neglected by the model and/or because τ_E is naturally decaying simultaneously with the field) or longer than that prediction (because the aircraft made its second or only pass too late, thus overestimating the observed decay time, or in the case of only a single late measurement, because τ_E was underestimated) without violating the model. The only way to avoid this dilemma is to find pairs of visits to cloud parcels both of which have elevated fields, so that they imply definite decay times rather than just upper bounds. Unfortunately, we have not found any such cases in the dataset that can be relied upon. All such cases have been discounted either because the wind velocity was not well enough known to identify re-visits or because there was evidence of continued development (and probable electrification) in the cloud.

The only set of explicit parcel re-visits that appears reasonably credible in this regard comes from 000614 (see Figure 31). Although none of these 7 re-visits violates model predictions, neither does any of them severely test the model. The apparent model violations between passes 1 and 2 on 010615 are ascribed to incorrect wind estimates, and a looser analysis of this storm appears consistent with the model. Although the re-visits that have been identified for 010604 and, especially, for 010624 may be credible in themselves (thus useful for examining the microphysical evolution of the cloud), both of these storms show evidence of "secondary development" that appears to be associated with local electrification. And although the time-of-flight analyses all appear consistent with the model, they cannot, by their nature, provide a critical test.

Neither does the statistical analysis lend a ringing endorsement to the model, although the relatively small number of "violators" (samples with τ_E < 1000 s but $|\boldsymbol{E}|$ > 2 kV/m) is the best evidence of model validity that we currently have (see the table on p.15). Previous conclusions of Dye et al. [2003] have been confirmed that τ_E is dominated by particles in the diameter range of 200 - 2000 μm (see Figure 5) but that the

concentrations of particles throughout the 3 - >1000 μm size range tend to be well correlated across the ensemble of anvil clouds (as indicated by moderately good correlations of τ_E with the other size ranges). The radar reflectivity, R_3, on the other hand, is dominated by particles larger than a millimeter (see Figure 12) but is nevertheless fairly well correlated with Log(τ_E) in anvil clouds (see Figure 14). Finally, the relationship of τ_E to |$\boldsymbol{E}$| exhibits a similar thresholding behavior to, but a better correlation than, the relationship of R_3 (and of other radar averages) to |$\boldsymbol{E}$| (compare Figures 15 and 17). The best relationship between τ_E and |$\boldsymbol{E}$| in the present dataset is obtained after filtering out anvils with low bases, anvils that may be precipitating, and anvils with nearby convective cores or nearby lightning (Figure 19). Nevertheless, the relationship between $N_{>1000}$ and |$\boldsymbol{E}$| exhibits just as high a correlation coefficient on this filtered dataset, although without the essential thresholding behavior (Figure 23).

Based on the above, I believe that it is reasonable to assume that the existing electrical-decay model is valid within its limitations. There is a considerable amount of consistency between observed and predicted field decays, which lends credence to the model, even though there are no critical tests. I do not see any promising prospects either for a more definitive validation or for an invalidation of this model using the present dataset.

"Secondary development," as described in the re-visit analysis of 010604, appears to be a fairly common phenomenon in long-lasting Florida anvils. Since it appears to be associated with local electrification (or re-electrification) of these anvils, it should be a concern for launch safety at KSC. As such, it probably merits further study.

Acknowledgments

I am especially grateful to Jim Dye and Sharon Lewis for identifying the flight intervals inside anvils, selecting the key storms to examine in detail, and providing the "30-s merged files" that were used in this study. This work would not have been possible without the dedicated field, calibration, and analytical efforts of the entire ABFM team. It was greatly facilitated by the timely presentation of ABFM results on the NCAR web site. Special thanks are also due to Phil Krider for his continuing encouragement, to Bill Hall for computing the 30-s-averaged microphysical data, and to Monte Bateman for providing relevant radial-velocity data from NEXRAD. Finally, I appreciate the opportunity provided by NASA/KSC to work on this interesting project.

List of *Additional* Symbols

R_3	Radar reflectivity averaged over a cube 3 km on a side centered on the aircraft location, also called AVGCUBE3X3 (dBZ)
$N_{3\text{-}55}$	Cloud-particle concentration in the size range between about 3 and about 55 µm diameter from the FSSP instrument, also called Con_FSSP (#/m^3)
$N_{100\text{-}200}$	Cloud-particle concentration in the size range between 100 and 200 µm diameter from the 2D-C probe, also called 2DC_100_200 (#/m^3)
$N_{200\text{-}1000}$	Cloud-particle concentration in the size range between 200 and 1000 µm diameter from the 2D-C probe, also called 2DC_200_1000 (#/m^3)
$N_{>1000}$	Cloud-particle concentration in the size range between 1000 and about 4000 µm diameter from the 2D-C probe, also called 2DC_GT_1000 (#/m^3)
$N'_{>1000}$	Cloud-particle concentration in the size range larger than 1000 µm diameter from the HVPS instrument, also called HVPS_GT_1000 (#/m^3)

References

Dye, J.E., W.D. Hall, S.A. Lewis, E. Defer, G. Dix, J.C. Willett, C.A. Grainger, P. Willis, M. Bateman, D. Mach, H. Christian, and F.J. Merceret, Microphysical properties and the decay of electric fields in Florida anvils, presented at the Fall Annual Meeting of the American Geophysical Union, San Francisco, CA, December, 2002.

Dye, J.E., W.D. Hall, J.C Willett, S. Lewis, E. Defer, P. Willis, D.M. Mach, M.G. Bateman, H.J. Christian, C.A. Grainger, J. Schild, and F.J. Merceret, The decay of electric field in anvils: observations and comparison with model calculations, in Proceedings, 12th International Conference on Atmospheric Electricity, Versailles, France, 9-13 June, International Commission on Atmospheric Electricity, 2003.

Willett, J.C., Electrical decay estimates in anvil clouds, Report No. 1 of 2 under Contract No. CC-90233B, submitted to the NASA Kennedy Space Center, 28 December, 2001.

Willett, J.C., and J.E. Dye, A simple model to estimate electrical decay times in anvil clouds, in Proceedings, 12th International Conference on Atmospheric Electricity, Versailles, France, 9-13 June, International Commission on Atmospheric Electricity, 2003.

Willett, J.C., Electrical decay estimates in anvil clouds, Report No. 2 of 2 under Contract No. CC-90233B, submitted to the NASA Kennedy Space Center, 11 April, 2003.